New insights into the role of porous microstructure on adiabatic shear localization

A. R. Vishnu, M. Marvi-Mashhadi, J. C. Nieto-Fuentes, J. A. Rodríguez-Martínez*

Department of Continuum Mechanics and Structural Analysis. University Carlos III of Madrid. Avda. de la Universidad, 30. 28911 Leganés, Madrid, Spain

Abstract

This paper provides new insights into the role of porous microstructure on adiabatic shear localization. For that purpose, we have performed 3D finite element calculations of electro-magnetically collapsing thick-walled cylinders. The geometry and dimensions of the cylindrical specimens are taken from the experiments of Lovinger et al. (2015), and the loading and boundary conditions from the 2D simulations performed by Lovinger et al. (2018). The mechanical behavior of the material is modeled as elastic-plastic, with yielding described by the von Mises criterion, an associated flow rule and isotropic hardening/softening, being the flow stress dependent on strain, strain rate and temperature. Moreover, plastic deformation is considered to be the only source of heat, and the analysis accounts for the thermal conductivity of the material. The distinctive feature of this work is that we have followed the methodology developed by Marvi-Mashhadi et al. (2021) to incorporate into the finite element calculations the actual porous microstructure of 4 different additively manufactured materials –aluminium alloy AlSi10Mg, stainless steel 316L, titanium alloy Ti6Al4V and Inconel 718– for which the initial void volume fraction varies between 0.001% and 2%, and the pores size ranges from ≈ 6 μm to ≈ 110 μm. The numerical simulations have been performed using the Coupled Eulerian-Lagrangian approach available in ABAQUS/Explicit (2016), which allows to capture the shape evolution, coalescence and collapse of the voids at large strains. To the authors' knowledge, this paper contains the first finite element simulations with explicit representation of the material porosity which demonstrate that voids promote dynamic shear localization, acting as preferential sites for the nucleation of the shear bands, speeding up their development, and tailoring their direction of propagation. In addition, the numerical calculations bring out that for a given void volume fraction more shear bands are nucleated as the number of voids increases, while the shear bands are incepted earlier and develop faster as the size of the pores increases.

Keywords:

Adiabatic shear bands, Porous microstructure, Thermal softening, Microstructural softening, Printed metals

*Corresponding author. E-mail address. jarmarti@ing.uc3m.es

1. Introduction

The problem of shear band localization in metallic materials subjected to high strain rates has drawn the attention of the Solid Mechanics community for almost a century (Zener and Hollomon, 1944). The concern on the shear banding phenomena comes from the fact that shear localization frequently precedes fracture of structural metals under dynamic loading conditions, e.g. during high-speed machining operations (Molinari et al., 2002; Burns and Davies, 2002; Ye et al., 2013), blast and explosions (Wiehahn et al., 2000), ballistic impact (Børvik et al., 2001; Zou et al., 2011) and high-velocity metalworking processes (Gaudillière, C. et al., 2010; Schmitz et al., 2020).

Many different experimental techniques have been developed over the last decades to study the mechanics of dynamic shear banding in a controlled laboratory environment. For instance, Hartley et al. (1987), Marchand and Duffy (1988) and Duffy and Chi (1992) used a Torsional Split Hopkinson Bar to twist thin-walled tubes at nominal strain rates ranging from 10^3 s^{-1} to $5 \cdot 10^3$ s^{-1}. The gauge section of the cylindrical specimens had a small thickness of 0.4 mm to assist in locating and localizing the shear deformation. The results obtained for various steel grades served to distinguish different stages in the process of nucleation and propagation of a shear band. At the beginning of loading, the strain field in the specimen was uniform; secondly, with the continuation of the loading process, after the maximum stress was attained, the strain started to localize with a continuous reduction in the width of the region over which the shear localization was occurring; and in the third stage the strain localized further, leading to the final fracture of the specimen. The advantage of the torsion experiments is that the thin-walled tube is subjected to simple shearing during the whole loading process, so that the strain and the strain rate are easily controlled (and determined), which facilitates the interpretation of results. Moreover, Ferguson et al. (1967) and Campbell and Ferguson (1970) devised a double shear specimen to be tested using a Split Hopkinson Bar apparatus which consists of two identical rectangular shear zones which connect a central portion loaded in compression and two supporting ends. Preventing lateral displacements of the supporting ends during loading –different designs of specimens and fixtures have been developed for that purpose over the years– it is possible to minimize the specimen bending and to obtain near simple shear deformations in the gauge sections (Klepaczko, 1994; Rusinek and Klepaczko, 2001; Guo and Li, 2012; Shi et al., 2014). The latest advances in this technique published by Xu et al. (2017, 2018, 2019a,b) enabled to study the shear deformation and fracture behaviors of 603 steel and pure Copper at strain rates up to 45000 s^{-1}. The stress and strain distributions were shown to be rather uniform in the central part of the shear regions of the sample during the loading process. However, the corners of the gauge sections acted as stress concentrators, promoting shear localization, so that the samples generally fractured along the diagonal directions of the shear zones. On the other hand, Meyer and Manwaring (1985) used a Split Hopkinson Pressure Bar to test axisymmetric hat-shaped specimens consisting of an upper hat part and a lower brim part, so that when subjected to compression the material between the hat and the brim parts shears. This technique enables to reach strain rates above 10^4 s^{-1}, and has the advantage of producing shear bands even in very ductile materials, making it possible to test metals and alloys with large differences in ductility using the same specimen geometry. The corners of the hat-shape specimen act as nucleation sites for the shear bands, so that even materials that do not show strain localization spontaneously can be forced up to shearing failure. This feature of the hat-shape sample has been exploited to study the mechanics of shear fracture in a variety of metals and alloys (Meyers et al., 1995; Nemat-Nasser et al., 1998; Andrade et al., 1994; Bronkhorst et al., 2006; Lins et al., 2007; Edwards et al., 2018; Lieou et al., 2019). However, this specimen design has the disadvantage that a high hydrostatic pressure evolves in the shear region during loading, so that the interpretation of the experimental results is not straightforward (see Peirs et al. (2010)). As an alternative to the hat-shaped sample, Rittel et al. (2002) developed the shear-compression specimen, which consists of a cylinder with two slots which are inclined with respect to the longitudinal axis, so that when loaded in compression, the gauge region of the specimen undergoes a dominant shear deformation, leading to the formation of a shear band at large strains. The shear-compression specimen is particularly attractive as it is easy to use in the standard Split Hopkinson Pressure Bar setup, and it has been successfully employed to study dynamic shear localization and fracture in different metallic materials (see Rittel et al. (2008a,b); Vural et al. (2003); Alkhader and Bodelot (2011); Dorogoy et al. (2015); Zhang et al. (2021)). However, the numerical analysis of the specimen showed that the stress state in the gauge section is three-dimensional, depends on the orientation of the slot, and evolves during loading (Vural et al., 2011; Dorogoy et al., 2015). In addition, the traction free boundaries at the edges of gauge section act as stress concentrators, favouring the shear fracture to start at these locations.

Note that the common basis for the experimental techniques described above is that they all refer to a state of forced shear localization (Lovinger et al., 2015), so that both the nucleation and the trajectory of the shear band –a single shear band is formed in these tests– are controlled by the specimen geometry and the loading conditions. This has advantages when it comes to obtain time and spatial resolved information of the shear localization process, yet the initiation of the shear band is dictated geometrically, and therefore externally forced, so that these experiments do not provide the true sensitivity of materials to shear localization.

In contrast, spontaneous shear localization can occur in radially symmetrical structures –like cylindrical specimens– when they are subjected to radially symmetrical loadings –e.g. internal or external pressures–, so that multiple shear bands can be formed at locations that generally cannot be predicted in advance. For instance, Nesterenko et al. (1989) developed the collapsing thick-walled cylinder technique in which a circular cross-section cylindrical specimen is subjected to rapid radial collapse under nearly plane strain conditions, so that the state of stress in the material approaches pure shear. The high pressures required for the collapse of the specimen are generated with the controlled detonation of an explosive charge located on the external wall of the cylinder. Multiple shear bands form spontaneously –and almost simultaneously– at large strains, being nucleated in the inner radius of the cylinder where the strain is maximum, and propagate towards the external radius, with the tips following a trajectory of maximum shear stress that makes a 45^0 angle to the radial direction (Gu and Ravichandran, 2005). The collapsing thick-walled cylinder technique was shown to produce controlled and repeatable helical shear band patterns, which allowed to investigate –for the first time– the collective behavior and spacing of shear bands at strain rates of $\approx 10^4$ s^{-1}. Experiments performed with Copper, AISI 304L, pure Titanium, Ti6Al4V and Tantalum specimens provided indications of the actual sensitivity of these materials to shear banding, and revealed that the critical strain leading to shear bands formation and the average separation between shear bands varies from material to material (Bondar and Nesterenko, 1991; Nesterenko and Bondar, 1994; Nesterenko et al., 1995, 1997, 1998; Xue et al., 2002, 2004). Similar conclusions were obtained from the recent experiments performed by Yang et al. (2011), Yang and Jiang (2016) and Yang et al. (2017) with different tempers of Ti-1300 titanium alloy and ZK60 magnesium alloy, which showed that the distribution, width, and spacing of the adiabatic shear bands varies with the heat treatment applied to the specimen before testing. Collapsing thick-walled cylinder experiments using an electromagnetic field as the driving collapsing force were performed by Stokes et al. (2001). When compared to the explosively driven experiments, the electromagnetic forces were shown to provide a more uniform collapse of the specimen. Recently, Lovinger et al. (2011, 2015) developed a electromagnetic set-up for the collapse of thick-walled cylinders at strain rates of $\approx 10^5$ s^{-1}, and tested seven metallic alloys with considerable differences in strength and ductility –AISI 304L, pure Titanium, wrought Ti6Al4V, additively manufactured Ti6Al4V, cast Al-A356, cast Mg-AM50 and OFHC Copper– in what probably is the most comprehensive experimental study on the formation of spontaneous shear bands published to date. Large differences in the number and length of the shear bands were obtained for the materials tested, being steel 304L, magnesium alloy AM50 and pure Titanium the materials with the greater failure strain and the smaller shear band spacing, while for OFHC Copper and aluminum alloy A356 no shear bands were observed. The experimental results, however, did not provide definite information to explain these differences, and the mechanisms which control shear localization are still are a source of active debate in the literature.

The classical explanation of Zener and Hollomon (1944) states that a shear band is formed when the thermal softening, caused by the local increase of temperature generated by plastic dissipation at high strain rates, overcomes the strain hardening of the material, leading to a rapid loss of the material capability to carry shear stress. The mechanisms involved in the development of the shear band are assumed to be cumulative, i.e., the high temperature band becomes progressively narrower, and ever higher strain rates and temperatures are attained in this narrowing band, which accelerates the localization process (e.g., see Wang et al. (1988), Zhou et al. (1996a,b) and Bonnet-Lebouvier et al. (2002)). This autocatalytic behavior, as it was named by Molinari and Clifton (1987), has motivated that the dynamic shear bands were accepted as a thermomechanical (material) instability, so that they have been customarily referred to as adiabatic shear bands. As stated by Molinari (1991), adiabatic shear bands usually form in materials with low thermal conductivity, in which the heat conduction does not refrain local heating. An alternative explanation to the formation of shear bands, which has been popularized following the work of Rittel et al. (2008a), states that the dynamic stored energy of cold work –the portion of the plastic work which is not dissipated into heat– causes microstructural softening evolutions leading to shear localization (e.g., see Osovski et al. (2012), Landau et al. (2016), Mourad et al. (2017), Lieou and Bronkhorst (2018), Lieou et al. (2019) and Magagnosc et al. (2021)). However, the idea that microstructural evolutions promote shear localization was introduced much earlier. For instance, Mathur and Backofen (1973) and Gil Sevillano et al. (1977) observed that texture evolution induced softening causes shear bands to form at large strains, as further substantiated by the finite element calculations reported by Dao and Li (2001), Kuroda and Tvergaard (2007) and Kuroda and Needleman (2019), among others. The shear bands in which thermal softening plays negligible role are commonly referred to as isothermal shear bands. Moreover, Dodd and Atkins (1983) theorized that for materials which contain voids –generally nucleated from inclusions, second phase particles and micro-cracks formed during materials manufacturing and processing– shear localization is possible due to the geometric softening induced by void distortion and inter-void interaction. The presence of elongated and coalesced voids inside the shear bands formed in the dynamic experiments of Bai et al. (1994), Xue et al. (2002), Odeshi et al. (2006), Yang et al. (2011) and Lovinger et al. (2015) substantiated the hypothesis of Dodd and Atkins (1983), and made apparent that in porous ductile materials dynamic shear localization is triggered by both thermal and geometric softening effects.

However, few efforts have been dedicated so far to incorporate the effect of porous softening on modeling dynamic shear bands. Kubair et al. (2015) performed 1D finite difference simulations of multiple shear band formation in a metallic specimen with preexisting voids and subjected to high strain rate. The mechanical behavior of the material was described with the constitutive model developed by Nahshon and Hutchinson (2008), who developed a phenomenological extension of the flow potential of Gurson (1977) to account for void evolution under shear deformation. It was shown that the porosity promotes early localization and reduces the shear bands spacing. The constitutive model of Nahshon and Hutchinson (2008) was also employed in the recent paper of Pascon and Waisman (2021) to perform 2D finite element calculations of two benchmark problems, a rectangular plate subjected to axial extension and a notched bar under tensile loading. Consistent with previous results of Kubair et al. (2015), the void shearing mechanism was found to accelerate material damage, leading to early shear band formation. A different constitutive framework to account for void induced softening on dynamic shear localization was employed by Dorothy and Longère (2019). These authors used the continuum damage mechanics approach proposed by Longère and Dragon (2016) to perform 3D finite element simulations of shear band formation in hat-shape specimens impacted at 30 m/s. The void softening effect was derived from a phenomenological potential which degrades the material properties as deformation evolves, so that the calculations showed that voids softening accelerates the propagation of shear bands. However, while the qualitative and quantitative results reported by Kubair et al. (2015), Pascon and Waisman (2021) and Dorothy and Longère (2019) are physically sound and seem to be consistent with the experimental evidence, it has to be noted that they were obtained using ad-hoc definitions of the effect of void softening in the formation and development of shear bands, i.e., the role of porosity on shear band localization was determined beforehand by the functional form of the constitutive relations employed. Note also that in the constitutive models of Nahshon and Hutchinson (2008) and Longère and Dragon (2016) the porosity is represented by a damage function which does not account for the effect of the spatial and size distributions of voids in the mechanical behavior of the material, disregarding the inherent heterogeneity of the porous microstructure of metals and alloys. These limitations of the approaches that are currently used to model the effect of void induced softening on dynamic shear banding have prevented from obtaining a complete understanding of the role of porosity on shear localization, showing the need for developing alternative methodologies which consider additional features of the materials' porous microstructure in the simulation of shear localization problems.

This is precisely the goal of this paper, in which we perform 3D finite element simulations of the formation of spontaneous multiple shear bands in collapsing thick-walled cylinders which contain populations of voids representative of the porous microstructure of four different additively manufactured materials. The voids are randomly distributed in the specimens, varying the initial void volume fraction between $\approx 0.001\%$ and $\approx 2\%$, and the pores size from ≈ 6 μm to ≈ 110 μm. The mechanical behavior of the material is modeled as elastic-plastic, with yielding described by the von Mises criterion, being the flow stress dependent on strain, strain rate and temperature. The numerical simulations have been performed using the Coupled Eulerian-Lagrangian approach available in ABAQUS/Explicit (2016), which allows to capture the shape evolution, coalescence and collapse of the voids at large strains. The geometry and dimensions of the cylindrical specimens, and the loading and boundary conditions, are taken from the experiments of Lovinger et al. (2015), and from the 2D simulations performed by Lovinger et al. (2018), respectively. To the authors' knowledge, this paper contains the first finite element simulations ever performed of the rapid collapse of thick-walled cylinders which include an explicit representation of the porous microstructure of the material, so that the effect of voids evolution on dynamic shear localization is unequivocally determined. Specifically, the calculations have shown that the pores favor early plastic localization, act as preferential sites for the nucleation of shear bands, speed up their development, and tailor their orientation.

2. Constitutive framework

The constitutive model used to describe the mechanical behavior of the collapsing cylinders follows the standard principles of von Mises (1928) plasticity. The rate of deformation tensor $\boldsymbol{d}$ is decomposed as the sum of an elastic part $\boldsymbol{d}^e$ and a plastic part $\boldsymbol{d}^p$:

$$\boldsymbol{d} = \boldsymbol{d}^e + \boldsymbol{d}^p \tag{1}$$

The relation between the elastic part of the rate of deformation tensor and the stress rate is given by the following hypo-elastic law:

$$\dot{\boldsymbol{\sigma}} = \boldsymbol{C} : \boldsymbol{d}^e \tag{2}$$

where $\dot{\boldsymbol{\sigma}}$ is an objective derivative of the Cauchy stress tensor –which corresponds to the Green-Naghdi rate in ABAQUS/Explicit (2016)– and $\boldsymbol{C}$ is the tensor of isotropic elastic moduli given by:

$$\boldsymbol{C} = 2G\tilde{\mathbf{I}} + K\mathbf{1} \otimes \mathbf{1} \tag{3}$$

where G is the elastic shear modulus, K is the bulk modulus, $\mathbf{1}$ is the second-order unit tensor and $\tilde{\mathbf{I}}$ is the fourth-order deviatoric unit tensor.

Moreover, the plastic part of the rate of deformation tensor is related to the Cauchy stress tensor by an associated flow rule:

$$\boldsymbol{d}^p = \dot{\lambda}\frac{\partial f}{\partial \boldsymbol{\sigma}} \tag{4}$$

where $\dot{\lambda}$ is the plastic flow proportionality factor and $f = \bar{\sigma} - \sigma_Y \leq 0$ is the yield function, with $\bar{\sigma} = \sqrt{\frac{3}{2}\boldsymbol{s} : \boldsymbol{s}}$ being the von Mises effective stress, where $\boldsymbol{s} = \boldsymbol{\sigma} - \sigma_h : \mathbf{1}$ and $\sigma_h = \frac{1}{3}\boldsymbol{\sigma} : \mathbf{1}$. Moreover, σ_Y is the yield stress of the material defined as:

$$\sigma_Y = \sigma_0(\bar{\varepsilon}^p + \varepsilon_0)^n \left(\frac{\dot{\bar{\varepsilon}}^p}{\dot{\varepsilon}_0}\right)^m \left(\frac{T}{T_0}\right)^\nu \tag{5}$$

where $\bar{\varepsilon}^p = \int_0^t \dot{\bar{\varepsilon}}^p(\tau)d\tau$ is the effective plastic strain, $\dot{\bar{\varepsilon}}^p = \sqrt{\frac{2}{3}\boldsymbol{d}^p : \boldsymbol{d}^p}$ is the effective plastic strain rate and T is the material temperature. The parameter σ_0 is the initial yield stress, and n, m and ν are the strain hardening, strain rate sensitivity and temperature sensitivity exponents, respectively. Moreover, ε_0, $\dot{\varepsilon}_0$ and T_0 are the reference strain, strain rate and temperature.

The energy equation is taken to be of the form:

$$\rho C_p \dot{T} = \beta\bar{\sigma}\dot{\bar{\varepsilon}}^p + k\nabla^2 T \tag{6}$$

where plastic dissipation is the only source of heat. Moreover, ρ is the current material density, C_p the specific heat, β the Taylor-Quinney coefficient and k the thermal conductivity.

The baseline constitutive parameters used in the calculations presented in Sections 5 and 6 correspond to Titanium and CRS 1018 Steel, and they are taken from Molinari (1997), see Table 1.

Symbol	Property and units	Titanium	CRS 1018 Steel
ρ_0	Initial density (kg/m^3)	4510	7800
G	Elastic shear modulus (GPa), Eq. (3)	43.28	78.85
K	Bulk modulus (GPa), Eq. (3)	120.83	170.83
C_p	Specic heat (J/Kg K), Eq. (6)	528	500
k	Thermal conductivity (W/m K), Eq. (6)	19	50
β	Taylor-Quinney coefficient, Eq. (6)	0.9	0.9
σ_0	Initial yield stress parameter (MPa), Eq. (5)	1171.45	639.77
n	Strain hardening exponent, Eq. (5)	0.15	0.015
m	Strain rate sensitivity exponent, Eq. (5)	0.033	0.019
ν	Temperature sensitivity exponent, Eq. (5)	-1.7	-0.38
ε_0	Reference strain, Eq. (5)	5.77×10^{-3}	5.77×10^{-3}
$\dot{\varepsilon}_0$	Reference strain rate (s^{-1}), Eq. (5)	0.001	0.001
T_0	Reference temperature (K) , Eq. (5)	293	293

Table 1: Numerical values of initial density, elastic constants, physical constants and parameters of the yield stress corresponding to Titanium and CRS 1018 Steel. Data after Molinari (1997).

3. Porosity distribution

In this section, we briefly recall the methodology developed by Marvi-Mashhadi et al. (2021) to determine the spatial and size distribution of pores present in four additively manufactured metals: aluminium alloy AlSi10Mg, stainless steel 316L, titanium alloy Ti6Al4V and Inconel 718.

Cylindrical specimens with diameter and height of 6 mm were printed by Selective Laser Melting by the company Materialise. In this paper, we only consider 4 out of the 12 samples investigated by Marvi-Mashhadi et al. (2021), namely: Al3XY, SS5XY, Ti0.5XY and INC1XY, where Al, SS, Ti and INC stand for the material, the following numbers indicate the nominal void volume fraction (%) provided by the manufacturer and XY tells that the samples were printed in parallel to the longitudinal axis of the cylinder. These four specimens are selected because they contain microstructures with large differences in void volume fraction, number of voids, average void size, and maximum void size, see Table 2, so that it is possible to obtain a clear depiction of the effect of porosity on the nucleation and collective behavior of shear bands at high strain rates. Moreover, analyzing 4 microstructures, instead of 12, facilitates the presentation of results. Note that in this paper the additively manufactured materials are solely employed to obtain representative porosity distributions to be used in the simulations of Sections 5 and 6;

the mechanical behavior of the collapsing cylinders being described by the constitutive model presented in Section 2 and the parameters of Table 1.

The porous microstructure of the printed materials was characterized by X-ray Computed Tomography (XCT). The reconstruction of the tomograms was performed using an algorithm based on the filtered back-projection procedure for Feldkamp cone beam geometry (e.g. see Stef et al. (2018)). Further analysis of 3D reconstructed images was performed using the open source software tool ImageJ (Schneider et al., 2012), so that for each sample we selected three cylindrical sub-volumes with diameter and height of 1.5 mm, with no overlapping between them, to obtain the spatial distribution, shape and size of the voids in the samples investigated. For all the specimens, the voids were roughly spherical and were rather homogeneously/uniformly distributed in the bulk of the material. Note that voids with diameter smaller than 6 μm could not be detected with the resolution of $3\times3\times3$ μm^3 of voxel size used in the X-ray tomography analysis. The experimental measurements for the void size distribution were fitted to a Log-normal statistical function with parameters given in Table 2.

	Al3XY	SS5XY	Ti0.5XY	INC1XY
VVF_0 (%)	2.17	0.0025	0.0013	0.0203
$Voids$ $(num./mm^3)$	5985	17	5	390
d_{max} (μm)	110.53	41.40	26.93	45.52
d_{min} (μm)	8.00	7.40	8.27	6.36
μ (μm)	15.98	11.21	17.30	6.41
dev (μm)	4.57	5.13	5.03	4.56

Table 2: Summary of the measurements obtained from the reconstructed 3D tomograms: initial void volume fraction (VVF_0), number of voids per mm^3 ($Voids$), maximum diameter of voids (d_{max}), minimum diameter of voids (d_{min}), and mean (μ) and standard deviation (dev) values of fitted Log-normal distribution. Results taken from Marvi-Mashhadi et al. (2021).

For a complete description of the X-ray tomography characterization of the porous microstructures considered in this work, including 3D reconstructions of the distribution of voids in the specimens, the reader is referred to Section 2 of Marvi-Mashhadi et al. (2021).

4. Finite element model

This section presents the 3D finite element model developed in ABAQUS/Explicit (2016) to investigate multiple shear banding in thick-walled cylinders subjected to rapid radial collapse. While this problem is customarily simulated using a 2D approach (Areias and Belytschko, 2007; Lovinger et al., 2011; Liu et al., 2016; Wang et al., 2020), in this paper we have developed a 3D version of the numerical model employed by Lovinger et al. (2018)

–which is based on the experimental setup of Lovinger et al. (2015)– in order to consider explicitly the porous microstructure of the specimen. The finite element model consists of three sandwiched cylinders: an inner copper cylinder (inner diameter 3.25 mm, outer diameter 3.5 mm), the specimen of the tested material (inner diameter 3.5 mm, outer diameter 5.0 mm) and an outer copper cylinder (inner diameter 5.0 mm, outer diameter 5.5 mm). Material points are referred to using a cylindrical coordinate system with positions in the reference configuration denoted as (R, Θ, Z). The origin of coordinates is located in the center of mass of the three coaxial cylinders, see Fig. 1. The outer boundary of the external copper cylinder is subjected to the same pressure load used in the simulations of Lovinger et al. (2018), which consists of half sinusoidal wave with an amplitude of 25 kbars and a duration of 2.2 μs. The inner copper cylinder controls the extend of the collapse and acts as a barrier to the formation of opening cracks. We have only analyzed one eighth of the coaxial cylinders in order to reduce the computational time, since very fine mesh is needed to capture the geometry of the porous microstructure of the specimen (see the discussion below). The lateral surfaces of the modeled portions of the three coaxial cylinders cannot move along the circumferential direction to maintain the axial symmetry of the problem, see Fig. 1. Similarly, the axial length of the coaxial cylinders is taken to be 0.25 mm (while in the experiments of Lovinger et al. (2011) varied between 15 mm and 30 mm), and their ends cannot move along the axial direction, so that the kinematics of the simulations is consistent with the nearly plane strain conditions obtained in the mid section of the cylinders in the experiments (Lovinger et al., 2011, 2018). Moreover, we assume that the dimensions of the numerical model enable to include sufficient number of voids in the specimen to obtain results which are representative of the porosity distributions investigated.

The novelty of the numerical shear banding analysis carried out in this paper is that we have included in the specimen the actual porous microstruture of four different additively manufactured materials, see Section 3. For that purpose, we have followed the methodology developed by Marvi-Mashhadi et al. (2021), assuming that the voids are spherical, and that they are randomly distributed in the material, consistently with the observations derived from the X-ray tomography analysis, see Section 3. The steps taken to generate the porous microstructure are as follows. Firstly, a Force Biased Algorithm (Bargieł and Mościński, 1991) is used to obtain a spatial distribution of M spheres, $\mathbb{S}(R_i, \Theta_i, Z_i, d_i)$, in a cubic volume element of $1{\times}1{\times}1$ mm^3, R_i, Θ_i and Z_i being the coordinates of the centers of the spheres and d_i the diameters of the spheres, where the sub-index i denotes the sphere number. The number of spheres and the distribution of spheres diameters are taken from the X-ray tomography measurements satisfying the Log-normal distribution with parameters given in Table 2. The intersection

	Al3XY	SS5XY	Ti0.5XY	INC1XY
Voids	1717±29	5±2	3±3	104±15

Table 3: Average number of voids and corresponding standard deviation (*Voids*) in the thick-walled cylindrical specimens modeled in ABAQUS/Explicit (2016) for the 4 microstructures investigated.

between spheres is not allowed, so that any overlapping ocurring during the generation of the microstructure is eliminated removing one of the overlapped spheres (the maximum number of spheres removed in this process is less than 2% of the total). This operation is repeated to obtain 5 random packed configurations of $1\times1\times1$ mm^3 which are placed next to each other –such that the whole specimen is included inside the arrangement of packed configurations– to generate the porous microstructure of the specimen. The spheres that lie outside the specimen boundaries, as well as the spheres overlapping with the boundaries of the specimen are dismissed, see Fig. 1. Next, the remaining spheres which lie inside the specimen boundaries are cut out to obtain actual voids in the finite element model. For each of the 4 porous microstructures considered (see Section 3) we have created three realizations of void size and position distribution which fulfill the same Log-normal statistical function, in order to take into account the scatter in the finite element results caused by the random spatial distribution of pores. These three realizations will be referred to as R1, R2 and R3. The average number of voids and the corresponding standard deviation included in the portion of the collapsing cylinders modeled, for the three realizations that we have generated per sample, and for the 4 microstructures investigated, are shown in Table 3. Note that the inner and outer copper rings are taken to be fully dense.

The numerical simulations have been performed using the Coupled Eulerian-Lagrangian approach available in ABAQUS/Explicit (2016) which allows to combine Lagrangian and Eulerian elements in the same analysis, so that while the inner and outer copper cylinders are modeled with Lagrangian elements, the specimen is considered to be Eulerian, see Fig. 2. Modeling the specimen as Eulerian material allows to capture the shape evolution, coalescence and collapse of the voids at large strains without the use of any failure criterion (Becker, 2017; Becker and Callaghan, 2020), and prevents from element distortion problems that appear in Lagrangian analysis involving extreme deformations –recall that in a Lagrangian analysis nodes are fixed within the material, so that the elements deform as the material deforms–. In an Eulerian analysis nodes are fixed in space, and material flows through elements that do not deform, so that the Eulerian mesh extends beyond the initial specimen boundaries, giving the material space in which to move and deform, see Fig. 2. Eulerian and Lagrangian parts of the finite element model interact each other through the Eulerian-Lagrangian contact, which is based on an enhanced immersed boundary

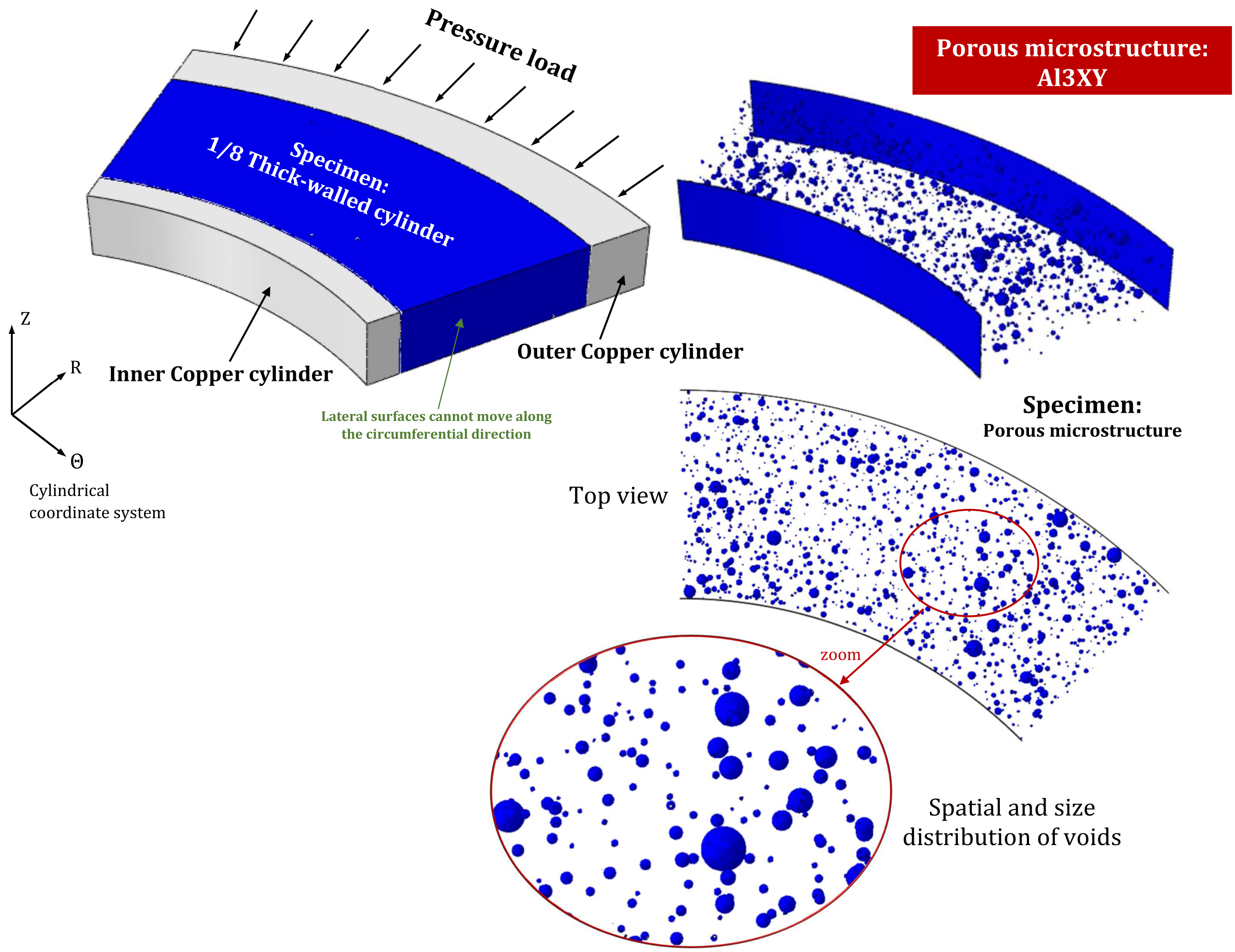

Figure 1: 3D finite element model developed in (ABAQUS/Explicit, 2016) to investigate multiple shear banding in thick-walled cylinders subjected to rapid radial collapse. The model consists of three sandwiched cylinders: an inner copper cylinder, the specimen and an outer copper cylinder. The pressure load is applied on the outer boundary of the outer copper cylinder. The specimens contains a spatial and size distribution of spherical voids representative of the microstructure Al3XY.

method (ABAQUS/Explicit, 2016). In this method, the Lagrangian mesh occupies void regions inside the Eulerian mesh. The contact algorithm automatically computes and tracks the interface between the Lagrangian and the Eulerian materials, and the contact constraints are enforced using a penalty method. The frictionless and hard pressure-overclosure contact constraint available in ABAQUS/Explicit (2016) has been used to define the contact between the Eulerian specimen and the Lagrangian copper cylinders. On the other hand, the Eulerian-to-Eulerian contact during the pores collapse occurs by default in ABAQUS/Explicit (2016) with a sticky behavior because of the kinematic assumption that a single strain field is applied to all materials within an element.

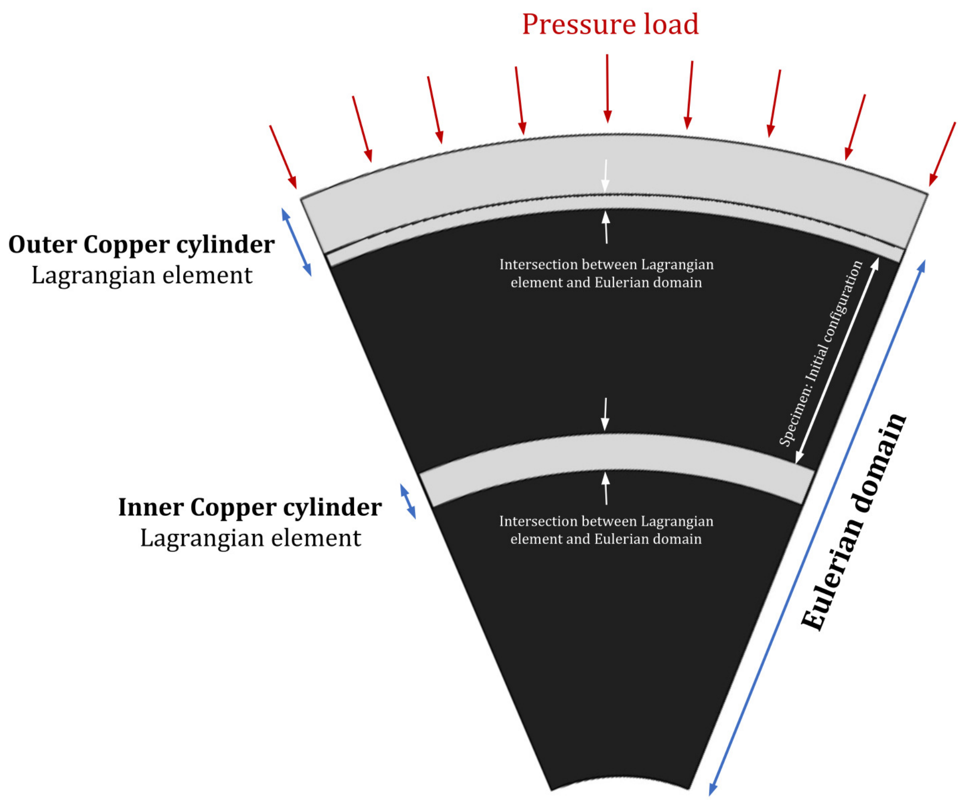

Figure 2: Top view of the 3D finite element model developed in ABAQUS/Explicit (2016) to investigate multiple shear banding in thick-walled cylinders subjected to rapid radial collapse. Identification of the Eulerian domain and the Lagrangian elements.

The Eulerian domain (specimen domain) is discretized with eight-node thermally-coupled solid Eulerian elements with reduced integration (EC3D8RT in ABAQUS notation), with initial dimensions $\approx 4{\times}4{\times}4\ \mu\mathrm{m}^3$. The volume fraction of material associated with each Eulerian element at the beginning of the computation has to be initialized –note that at a particular time step, a single Eulerian element can contain material, void or both– using the Volume Fraction Tool available in ABAQUS. Moreover, the inner and outer copper cylinders are discretized with eight-node thermally-coupled solid elements, with reduced integration and hourglass control (C3D8RT in ABAQUS notation), with dimensions $\approx$ 10$\times$10$\times$10 μm^3, so that the whole finite element model contains $\approx$ 16 million elements. The calculations were performed using two workstations with 12 and 48 cores, respectively, with the following features Intel Xeon Gold 6128 @ 3.7 GHz and Intel Xeon Gold 5220R @ 4.0 GHz. The computational cost of each simulation shown in this paper ranged between 3 and 7 days, depending on the the loading velocity, the material behavior and the microstructure considered, using simultaneously all the cores of the workstations indicated before.

A key point for the analysis is to obtain the evolution of the void volume fraction in the specimen during the simulations. For that purpose, we have developed the following two-steps methodology.

1. The matrix material volume, MMV, at each time step, is computed as.

$$MMV = \sum_{n=1}^{n_{elem}} MVF_n \times EVOL_n \tag{7}$$

   where, n_{elem} is the number of Eulerian elements, and MVF and $EVOL$ are the material volume fraction and the volume of the corresponding Eulerian element, respectively.

2. Top-view and bottom-view screenshots of the sample are exported to MATLAB® as greyscale images with contrasting background. Images obtained for all time steps are processed using the Image Processing module of MATLAB® to find the area of the specimen contained in the R - Θ plane in both top-view and bottom-view. We assume a linear variation of the area in the axial direction (since there is a small difference between the areas of both the surfaces after shear bands are formed). The total volume, V, at each time step, is then approximated by multiplying the calculated average area of the top and bottom surfaces by the axial length of the specimen (0.25 mm).

The void volume fraction, VVF, at each time step, is then computed as.

$$VVF = \frac{V - MMV}{V} \tag{8}$$

The constitutive behavior of the specimen presented in Section 2 has been implemented into ABAQUS/Explicit

(2016) through a user subroutine VUMAT. Moreover, the constitutive model used for the inner and outer copper cylinders is preimplemented in ABAQUS/Explicit (2016) and consists of linear elasticity and von Mises plasticity with hardening described by the Johnson-Cook model (Johnson and Cook, 1983). The material parameters for copper are taken from Table 1 of Lovinger et al. (2018).

5. Salient results

The finite element simulations reported in this section correspond to Titanium, see Table 1. In Section 5.1, we compare calculations performed with fully dense material and with porous microstructure Al3XY for realization R1. The results illustrate the effect of actual voids on dynamic shear localization. Note that the microstructure Al3XY contains the larger amount of voids, and the greater voids, among the porous microstructures considered, see Table 3. Section 5.2 compares results obtained with realizations R2 and R3 of the microstructure Al3XY. The topology of the porosity distribution is shown to affect the localization pattern and the specific locations where the shear bands nucleate. In Section 5.3, we perform calculations with realization R2 of porous microstructure Al3XY for different values of the temperature sensitivity exponent ν, see Table 1. The results bring to light the influence of thermal softening on dynamic shear localization in porous materials.

5.1. The comparison between porous and fully dense materials

Fig. 3 shows contours of effective plastic strain $\bar{\varepsilon}^p$ for microstructure Al3XY and realization R1. Four different loading times are considered. $t = 0.5$ μs, 1 μs, 1.5 μs and 2 μs. The color coding of the isocontours is such that effective plastic strains ranging from 0 to 1.5 correlate with a color scale that goes from blue to red. Effective plastic strains above 1.5 remain red. Note that the inner and outer copper cylinders are not shown. Subplots (a)-(b)-(c)-(d) correspond to *solid representations* of the specimen which illustrate the formation and development of multiple shear bands, while subplots (d)-(f)-(g)-(h) correspond to *empty representations* of the specimen which show the evolution of the porous microstructure. For $t = 0.5$ μs the distribution of plastic strains in the specimen is largely homogeneous, the deformation gradients being imperceptible for the colour scale used to represent the isocontours. The microstructure remains virtually undeformed with the pores being almost spherical. For $t = 1$ μs we observe the onset of plastic localization in specific locations of the specimen which correspond to the position of large voids and clusters. The zoomed areas of the porous microstructure display deformed voids leading to geometric softening and promoting localization (e.g. see Nahshon and Hutchinson (2008) and the discussion in the following paragraphs). The nucleation of multiple shear bands in the inner radius of the specimen becomes apparent for $t = 1.5$ μs. Consistent with experiments reported elsewhere (Nesterenko et al., 1995; Lovinger et al., 2011), the shear bands propagate towards the external radius of the sample, along trajectories that make a $\approx 45^0$ angle to the radial direction. The zoomed area of the microstructure shows that the voids are elongated and sheared, finding close resemblance with the shape of the pores observed inside shear bands in the collapsing thick-walled experiments of Xue et al. (2002) and Lovinger et al. (2015) –see Figs. 8 and 9 therein–. For a loading time of 2 μs, the specimen contains multiple shear bands with different degrees of development. The shear bands intersect each other, displaying irregular trajectories modulated by the porous microstructure (intervoid interaction, as stated by Dodd and Atkins (1983)), leading to a topological shear bands distribution originated from the spatial distribution of voids (shear bands are linking the voids, as in the experiments with voided materials of Weck et al. (2006)). The intersection of shear bands occurs near large pores and clusters that triggered early plastic localization (as mentioned before) and at the boundaries of the specimen (edge effects, e.g. see Zaera et al. (2015)). For this loading time, the void volume fraction has been significantly reduced (see Fig. 8 and the discussion therein), and many pores have collapsed, specially near the outer radius of the specimen. The closure of pores is caused by the hydrostatic pressure that develops in the specimen during loading (which is most likely attributed to dynamic effects).

Fig. 4 shows contours of effective plastic strain for the fully dense material. No voids are included in the finite element model, and the small round-off errors present in the nodal coordinates, and the errors associated to the numerical integration of the balance laws and the constitutive equations, are responsible for breaking the symmetry of the problem and triggering localization (see the finite element calculations performed by Guduru and Freund (2002) and Rusinek and Zaera (2007), among others, for ring expansion problems in which numerical perturbations trigger the formation of multiple necks along the circumference of the specimen). Similar strategy was followed by Lovinger et al. (2018), who performed 2D calculations of collapsing thick-walled cylinders with a Lagrangian hydrocode in which the unstructured mesh used to discretize the specimen was responsible for breaking the symmetry of the problem. Lovinger et al. (2018) showed that, while the initial perturbations acted as a trigger for the localization to occur, the shear bands distribution was eventually determined by the waves travelling along the circumference of the cylinder and by the mechanical behavior of the material. The colour coding is the same used in Fig. 3, however, the contours correspond to greater loading times, namely $t = 2$ μs, 2.5 μs, 3 μs and 3.5 μs, showing that the localization process is delayed for the fully dense material (i.e., porosity favours shear localization). For $t = 2$ μs, the plastic flow has not localized yet, so that the plastic strains increase smoothly towards the inner radius of the specimen. Note that for the same loading time the shear bands pattern was fully

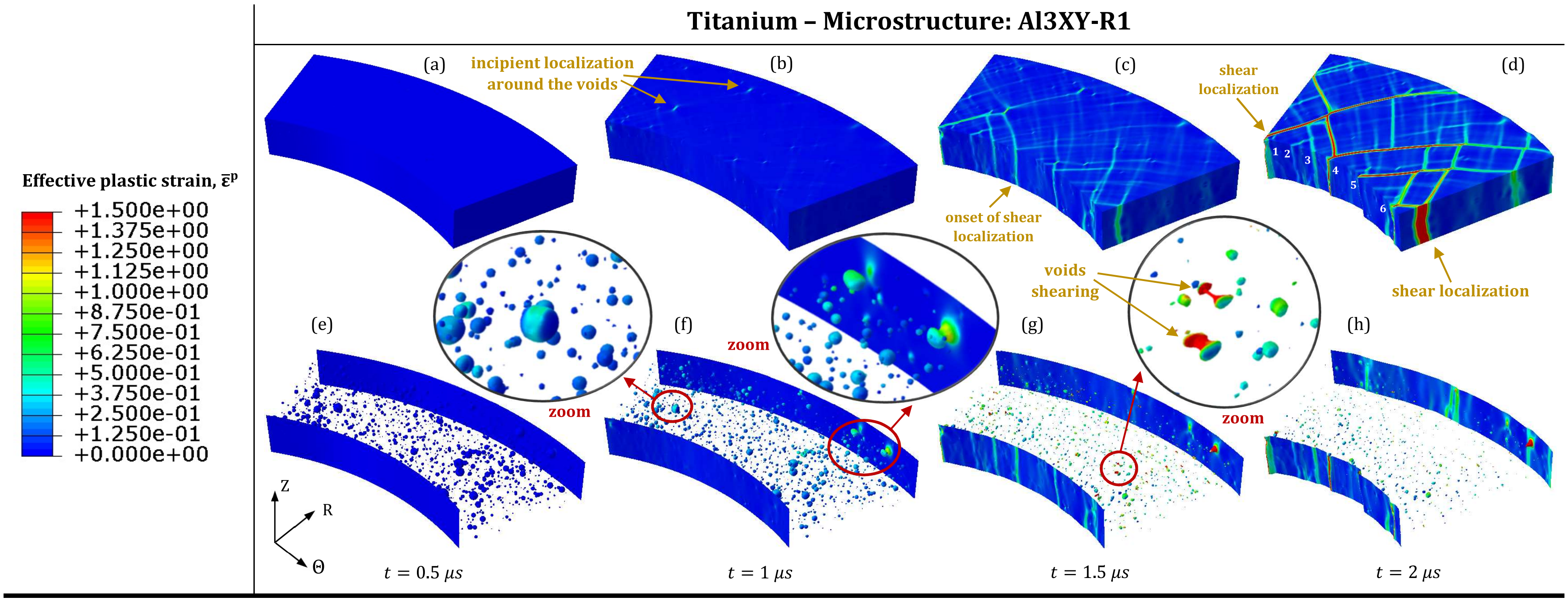

Figure 3: Results corresponding to Titanium with microstructure Al3XY and realization R1. Contours of effective plastic strain $\bar{\varepsilon}^p$ for different loading times: (a)-(e) $t = 0.5$ μs, (b)-(f) $t = 1$ μs, (c)-(g) $t = 1.5$ μs and (d)-(h) $t = 2$ μs. Subplots (a)-(b)-(c)-(d) correspond to *solid representations* of the specimen which show the formation and development of multiple shear bands. Subplots (d)-(f)-(g)-(h) correspond to *empty representations* of the specimen which show the evolution of the porous microstructure.

formed for the microstructure Al3XY–R1, see Fig. 3(d). With the continuation of the loading process, a series of shear bands become visible for $t = 2.5$ μs. These bands further develop to form at $t = 3$ μs an array of spiral shear bands which progress towards the outer radius of the specimen. At $t = 3.5$ μs the effective plastic strain inside the shear bands is above 4. Note that the shear bands for the fully dense material are more regularly spaced than in the case of the microstructure Al3XY–R1, and their degree of development is also more uniform –compare Figs. 3(d) and 4(d)–.

Quantitative results of the development of the shear bands patterns are provided in Fig. 5, which shows the evolution of the effective plastic strain $\bar{\varepsilon}^p$ in the inner radius of the specimen with the normalized inner perimeter (also referred to as normalized radial angle in the figures) of the ring $\bar{P} = \frac{4\theta}{\pi}$ for the porous microstructure Al3XY–R1 and the fully dense material, Figs. 5(a) and 5(b), respectively. The loading times are the same considered in Figs. 3 and 4. The y-axis scale is half in Fig. 5 (a) because plastic localization occurs earlier in the porous material. Note that for the porous microstructure the effective plastic strain attains a maximum value of ≈ 2 at 2 μs, while for the fully dense material this level of strain is reached at 3 μs (see the dashed yellow lines). The $\bar{\varepsilon}^p$ - $\bar{P}$ curves, which are roughly horizontal at the beginning of loading (see the dashed blue curves), eventually display a succession of peaks and valleys for later loading times, where the peaks denote the formation of shear bands. Consistent with the observations derived from Figs. 3 and 4, while the number of shear bands (peaks) is larger in the case of the porous microstructure, their relative degree of development (relative height of the peaks) is more heterogeneous. Assuming that each peak represents a shear band, the average shear bands spacing for the porosity distribution Al3XY–R1 (14 peaks at $t = 2$ μs), referred to the undeformed configuration, is ≈ 0.2 mm. This value is in reasonable agreement with the experimental measurements of Xue et al. (2002) and Lovinger et al. (2015), who reported values for the spacing of ≈ 0.18 mm and ≈ 0.21 mm, respectively, for commercial pure Titanium, and ≈ 0.53 mm and ≈ 0.46 mm for Ti6Al4V. The most developed shear bands, 6 in the case of the porous microstructure and 7 in the case of the fully dense material, are indicated in the graphs, and in the contour plots of Figs. 3(d) and 4(d).

5.2. The comparison between different microstructural realizations

Fig. 6 compares contour plots of effective plastic strain for calculations performed with the porous microstructure Al3XY and realizations R2 and R3. The results correspond to two different loading times, 1 μs and 2 μs. Qualitatively, the number, distribution and degree of development of the shear bands is similar for both realizations. The localization patterns are irregular, so that the shear bands intersect and branch/bifurcate as they propagate towards the outer radius of the specimen, showing a definite resemblance with the experimental ob-

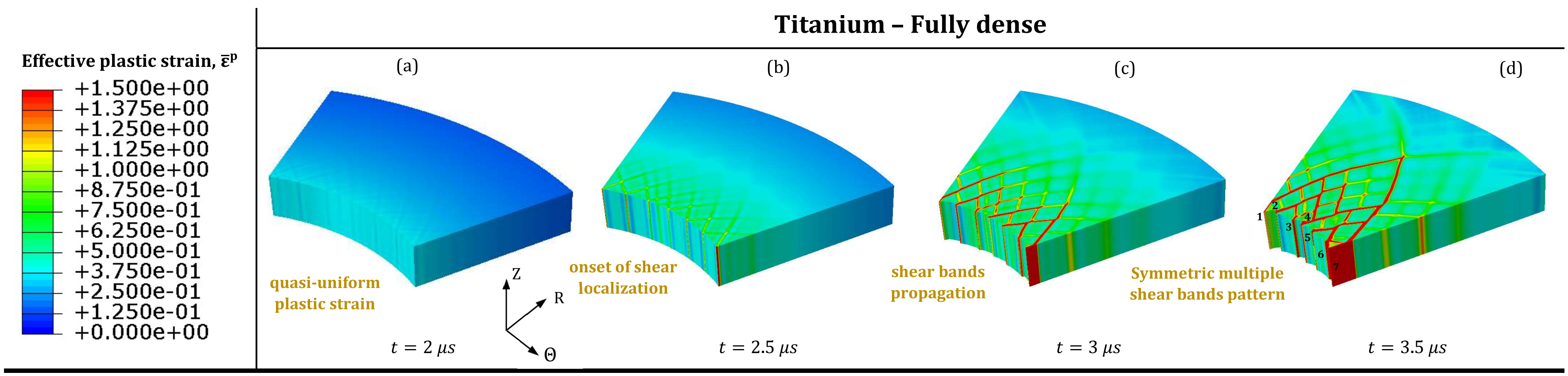

Figure 4: Results corresponding to fully dense Titanium. Contours of effective plastic strain $\bar{\varepsilon}^p$ for different loading times: (a) $t = 2$ μs, (b) $t = 2.5$ μs, (c) $t = 3$ μs and (d) $t = 3.5$ μs.

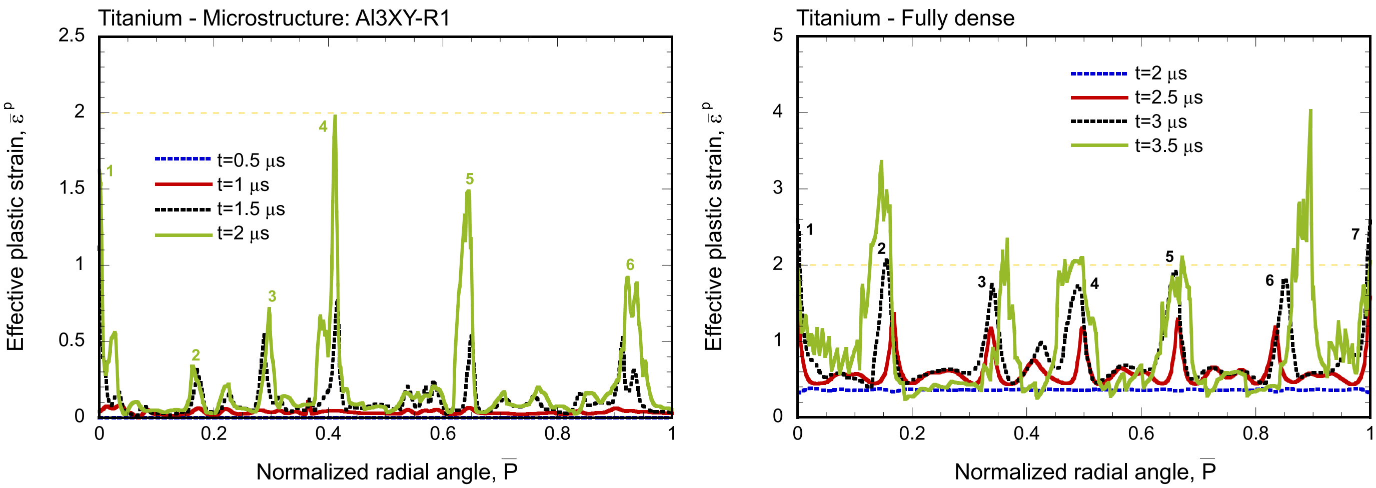

(a) (b)

Figure 5: Results corresponding to Titanium. Effective plastic strain $\bar{\varepsilon}^p$ versus normalized inner perimeter of the ring $\bar{P} = \frac{4\theta}{\pi}$. (a) Microstructure Al3XY and realization R1. Four different loading times: $t = 0.5$ μs, 1 μs, 1.5 μs and 2 μs. (b) Fully dense material. Four different loading times: $t = 2$ μs, 2.5 μs, 3 μs and 3.5 μs. The horizontal yellow dashed lines correspond to $\bar{\varepsilon}^p = 2$. For interpretation of the references to color in this figure, the reader is referred to the web version of this article.

servations reported, for instance, in Fig. 2(c) of Nesterenko et al. (1995). However, the specific locations where the shear bands nucleate are different for R2 and R3, see the position of the excursions of strain which represent shear localization sites in the $\bar{\varepsilon}^p$ - $\bar{P}$ curves of Fig. 7. This reinforces the idea that the spatial distribution of voids affects the topology of the localization pattern. The average shear bands spacing referred to the undeformed configuration for realizations R2 and R3 is ≈ 0.23 mm and ≈ 0.21 mm, respectively (assuming that each peak of strain represents a shear band). Moreover, the evolution of the porous microstructure is also similar for both realizations (compare plots 6(c)-(b) and 6(g)-(h)). Namely, a quantitative measure for the microstructure evolution is provided in Fig. 8, which shows the normalized void volume fraction $\overline{VVF} = \dfrac{VVF}{VVF_0}$ as a function of the loading time t. The decreasing value of $\overline{VVF}$ over time illustrates that the pores close during loading. Note that the results for the two realizations are very similar, which suggests that, despite the different spatial and size distribution of voids, the overall response of the specimen for different realizations of the same microstructure is virtually the same (the number of shear bands for different realizations is also very similar, as shown above). The voids deform during loading, as illustrated by the zoomed area of Fig. 6 (g) and the sequence of plots of Fig. 9, which show the evolution of a set of voids of realization R3 for a time interval spanning from 1 μs to 1.5 μs. A shear band goes through the two larger voids, so that the pores become heavily distorted and split up into two smaller cavities that eventually collapse with the continuation of the loading process. The shape evolution of the voids in Fig. 9 finds reasonable qualitative agreement with the experimental observations reported by Weck et al. (2006) for voided materials which display shear localization bands linking the voids.

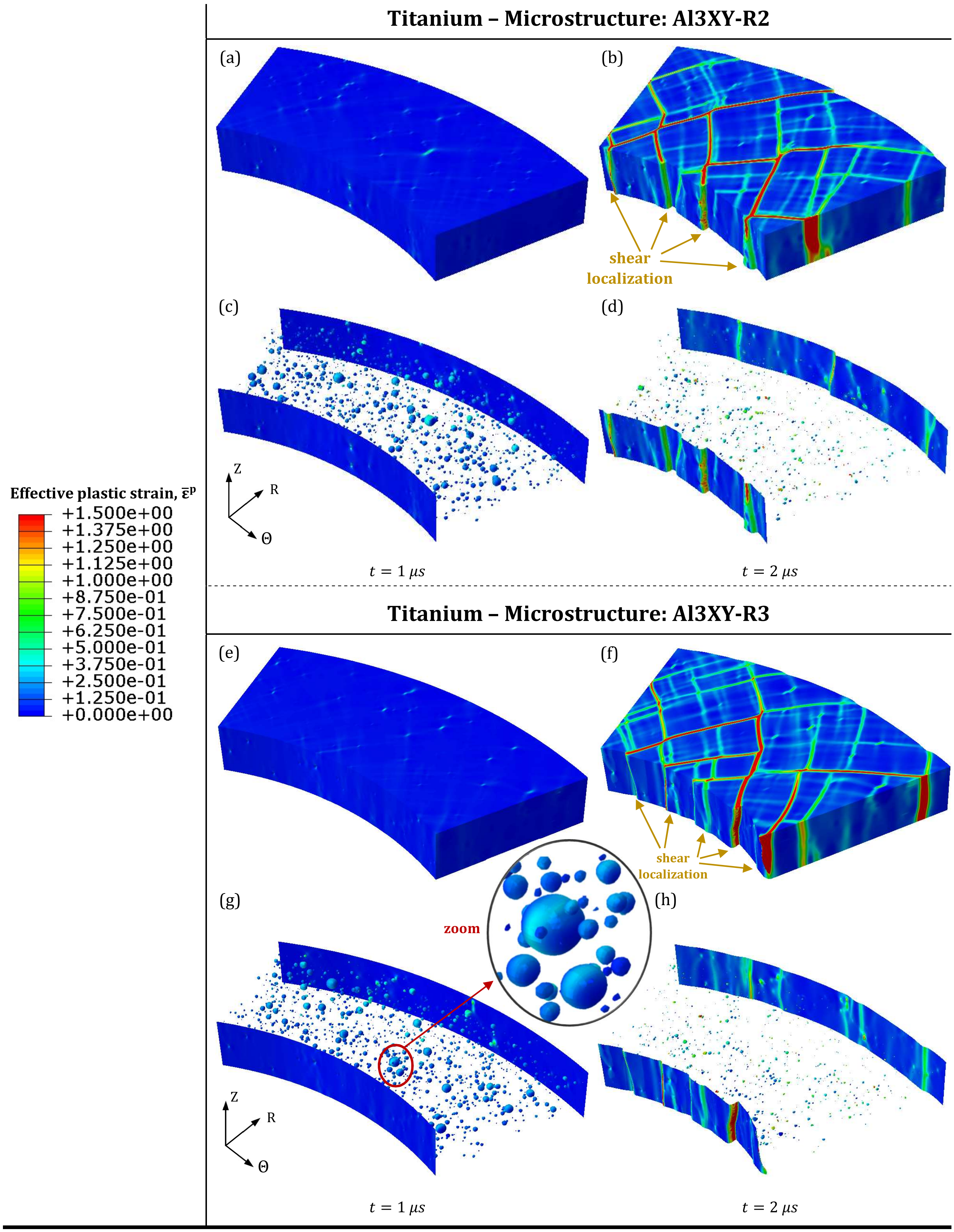

Figure 6: Results corresponding to Titanium with microstructure Al3XY for two different loading times $t = 1\ \mu$s and $t = 2\ \mu$s. Subplots (a)-(b)-(c)-(d) correspond to realization R2 and subplots (e)-(f)-(g)-(h) to realization R3. *Solid representations* of the specimens show the formation and development of multiple shear bands and *empty representations* show the evolution of the porous microstructure.

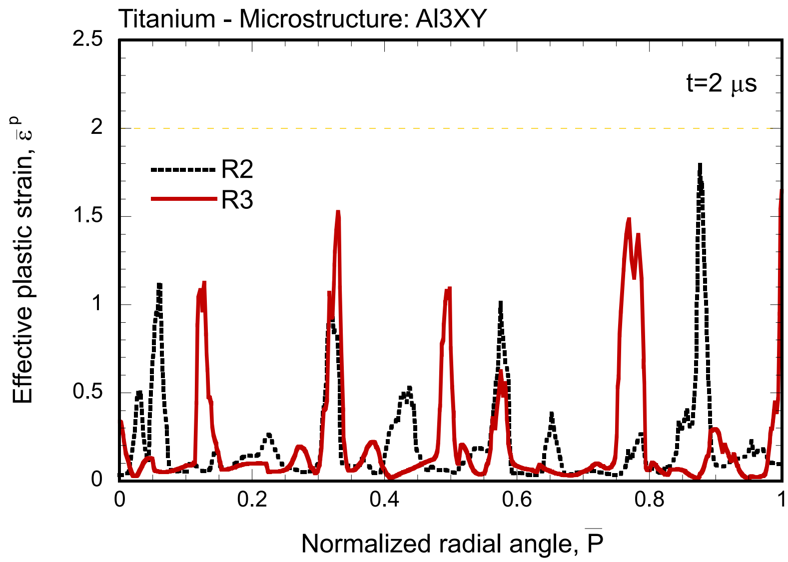

Figure 7: Results corresponding to Titanium. Effective plastic strain $\bar{\varepsilon}^p$ versus normalized inner perimeter of the ring $\bar{P} = \frac{4\theta}{\pi}$ for microstructure Al3XY and realizations R2 and R3. The loading time is $t = 2$ μs. The horizontal yellow dashed line corresponds to $\bar{\varepsilon}^p = 2$.

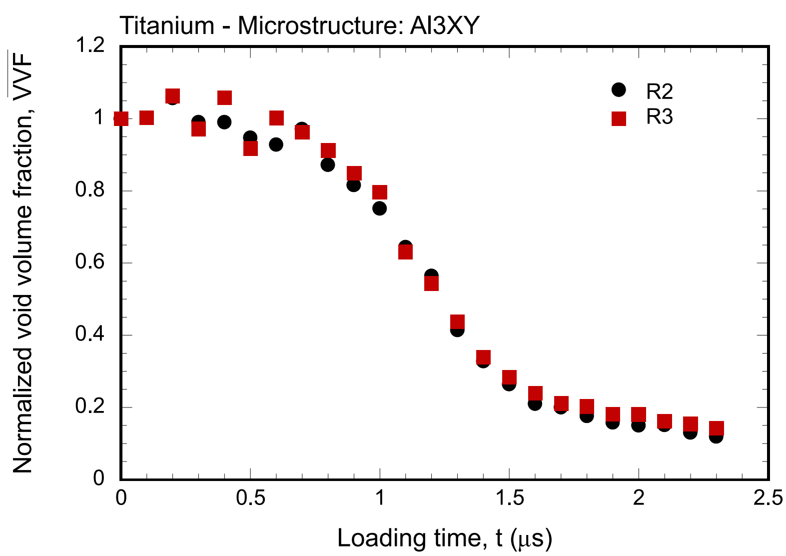

Figure 8: Results corresponding to Titanium with microstructure Al3XY. Evolution of the normalized void volume fraction $\overline{VVF} = VVF/VVF_0$ with the loading time t for two realizations R2 and R3.

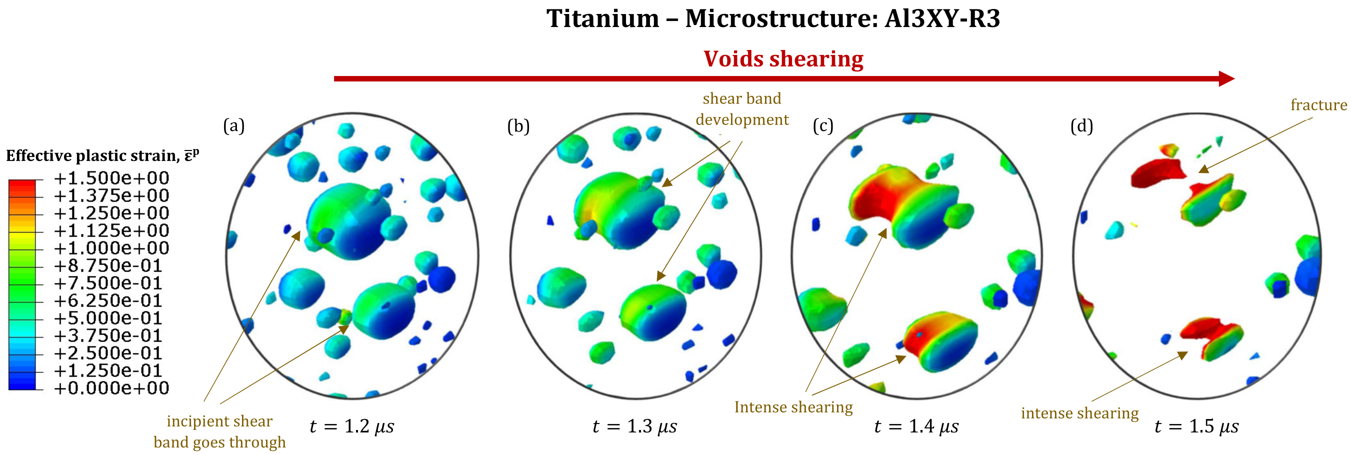

Figure 9: Results corresponding to Titanium with microstructure Al3XY and realization R3 for four different loading times: (a) $t = 1.2$ μs, (b) $t = 1.3$ μs, (c) $t = 1.4$ μs and (d) $t = 1.5$ μs. Detail of voids shearing process.

5.3. The interplay between porous microstructure and thermal softening

Fig. 10 shows contour plots of effective plastic strain for calculations with microstructure Al3XY–R2 performed for different values of the temperature sensitivity parameter $\nu = -1, -0.5$ and 0 (temperature independent material). Note that these values are smaller than the reference parameter of Table 1. Moreover, the color coding of the contour plots is the same used in Figs. 3, 4, 6 and 9. The isocontours for $\nu = -1$, Figs. 10(a)-(b), correspond to two different loading times, $t = 2$ μs and 2.5 μs, respectively. The comparison of the effective plastic strain field obtained for $t = 2$ μs with the results reported for the same microstructure realization, the same loading time, and $\nu = -1.7$ in Fig. 6 (b) shows that decreasing the temperature sensitivity exponent delays shear localization. The isocontours for $\nu = -0.5$ are shown in Figs. 10(c)-(d), and correspond to $t = 3$ μs and 3.5 μs, respectively. In comparison with the results obtained for $\nu = -1$, the distribution of plastic strains in the specimen is more homogeneous, i.e., the localization of plastic deformation is less intense, and the shear bands are less developed and shorter (they propagate shorter distance from the inner radius of the specimen). These results make apparent the role of thermal softening on shear bands localization in porous materials. The isocontours for the temperature independent material $\nu = 0$ are shown in Figs. 10(e)-(f) for the same loading times considered for $\nu = -0.5$ (note that at $t = 3.8$ μs for the temperature independent material the inner copper cylinder gets fully collapsed and the specimen cannot keep deforming). The plastic strain increases from the inner radius of the specimen towards the external perimeter without clear indications of the formation of shear bands. While porosity favors and accelerates shear bands formation and development, these results suggest that thermal softening is required to trigger localization (at least for the specific problem and material behaviors considered in this paper).

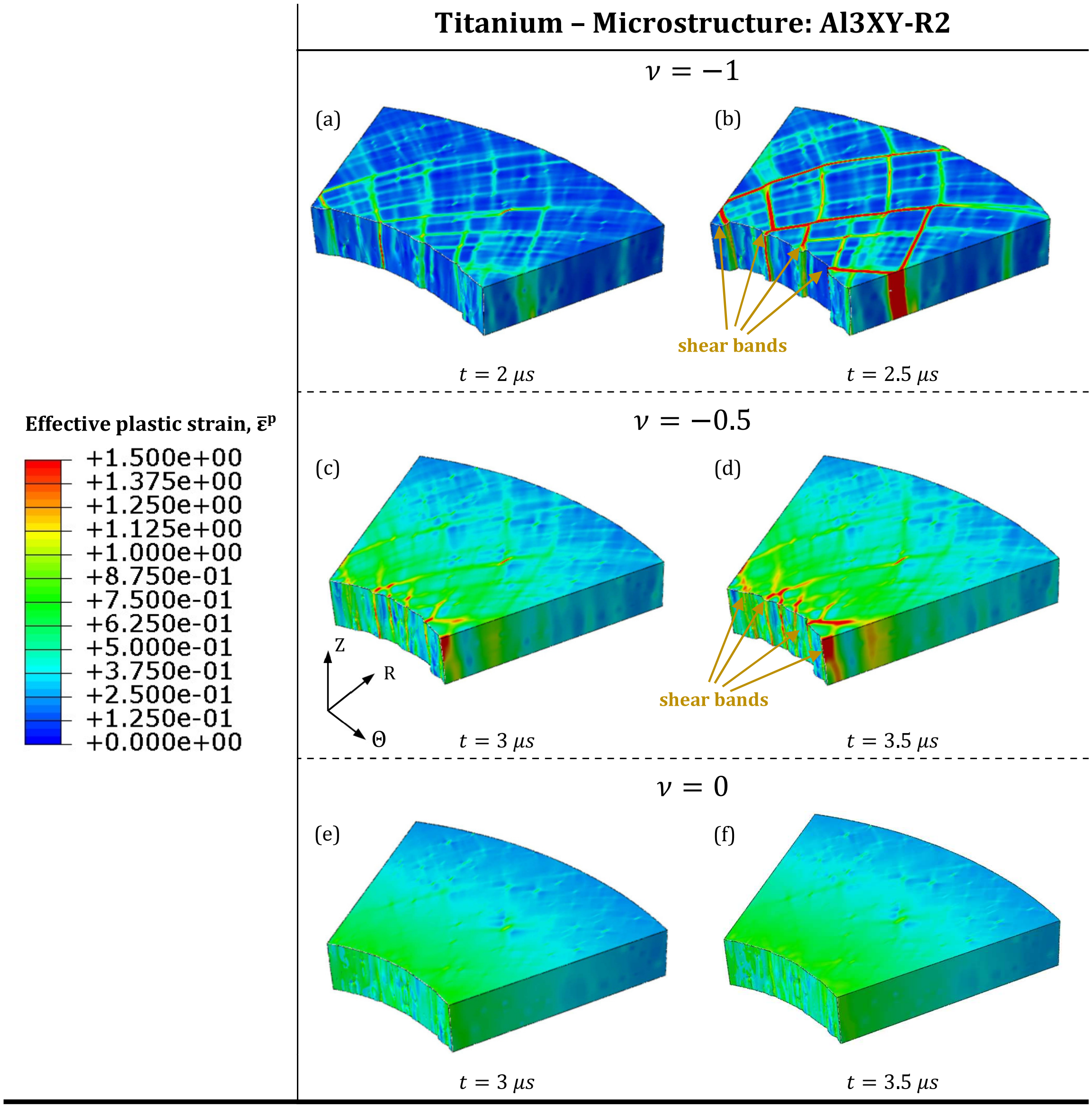

Figure 10: Results corresponding to Titanium with microstructure Al3XY and realization R2. Contours of effective plastic strain $\bar{\varepsilon}^p$ for three different values of the temperature sensitivity exponent: (a)-(b) $\nu = -1$ for two different loading times $t = 2$ μs and 2.5 μs, (c)-(d) $\nu = -0.5$ for two different loading times $t = 3$ μs and 3.5 μs, and (e)-(f) $\nu = 0$ (temperature independent material) for two different loading times $t = 3$ μs and 3.5 μs.

The critical role of thermal softening on shear banding is further exposed in Fig. 11 which shows the evolution of the effective plastic strain $\bar{\varepsilon}^p$ versus the normalized inner perimeter of the ring $\bar{P}$ for $\nu = -1$, -0.5 and 0 (temperature independent material). The loading times corresponding to the three values of ν –indicated in the plot– are selected so that the maximum value of the effective plastic strain is ≈ 1 (recall that for the temperature independent material $t = 3.8$ μs is the maximum loading time attained in the simulation before the inner cylinder collapses). The *saw-like* profile of the $\bar{\varepsilon}^p$ - $\bar{P}$ curves is more pronounced as the absolute value of ν increases, showing that thermal softening promotes earlier and faster shear localization. In fact, for the temperature independent material, despite the loading time is greater, the difference in plastic strain from peaks to valleys is comparatively small, and the width of the strain excursions is comparatively large, which explains that no shear bands appear in the contour plots of Fig. 10. In absence of thermal softening, the shear localization is diffuse –leading to diffuse shear localization regions– and the number of peaks is less than for the materials which display thermal softening. Moreover, note that for $\nu = -1$ and -0.5 the location of most strain excursions is the same –the only noticeable discrepancy is indicated with a blue arrow–, which suggests that for this porous microstructure, while thermal softening is essential to trigger localization, the spatial distribution of the shear bands is largely controlled by the distribution of voids (while the porous microstructure may have less influence on the distribution of shear bands if the void volume fraction is less, the voids are smaller, and inertia and strain rate sensitivity are more, this discussion is left for a future work).

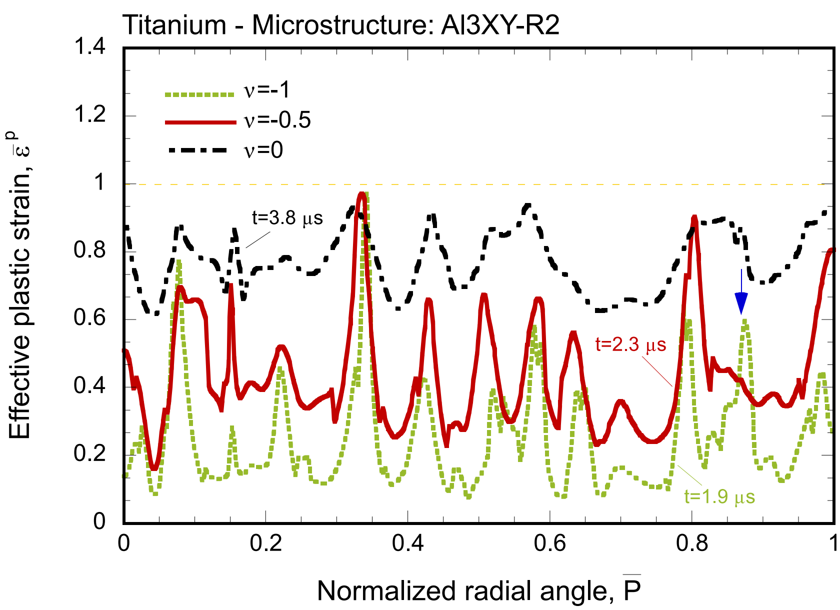

Figure 11: Results corresponding to Titanium with microstructure Al3XY and realization R2. Effective plastic strain $\bar{\varepsilon}^p$ versus normalized inner perimeter of the ring $\bar{P} = \frac{4\theta}{\pi}$ for three different values of the temperature sensitivity exponent: $\nu = -1$, $\nu = -0.5$ and $\nu = 0$ (temperature independent material). The loading time is selected so that the maximum value of the effective plastic strain is ≈ 1. The horizontal yellow dashed line corresponds to $\bar{\varepsilon}^p = 1$. For interpretation of the references to color in this figure, the reader is referred to the web version of this article.

The temporal evolution of the void volume fraction for the same calculations of Figs. 10 and 11 is pictured in Fig. 12. The rate of collapse of the pores is similar for the three values of ν considered up to ≈ 1.1 μs, while for greater loading times the decrease of $\overline{VVF}$ is slower for the temperature independent material. The influence of thermal softening on the evolution of the porous microstructure is further illustrated in Fig. 13, which shows contours of effective plastic strain for the specimens corresponding to $\nu = -1$ and $\nu = 0$ with visualization of the porous microstructure. For this loading time, $t = 2$ μs (see dashed yellow line in Fig. 12), it is apparent that the pores are bigger in the case of the temperature independent material, suggesting that thermal softening favors early closure of the voids. Moreover, while the comparison is not explicitly shown for the sake of brevity, we have also checked that the decrease of $\overline{VVF}$ with loading time is even faster in the case of $\nu = -1.7$ (results depicted in Fig. 8) than in the cases of $\nu = -1$ and –0.5 (results shown in Fig. 12), so that as the thermal softening increases, the rate of collapse of the voids occurs more rapidly. It seems that rapid voids closure indicates/favors early shear localization.

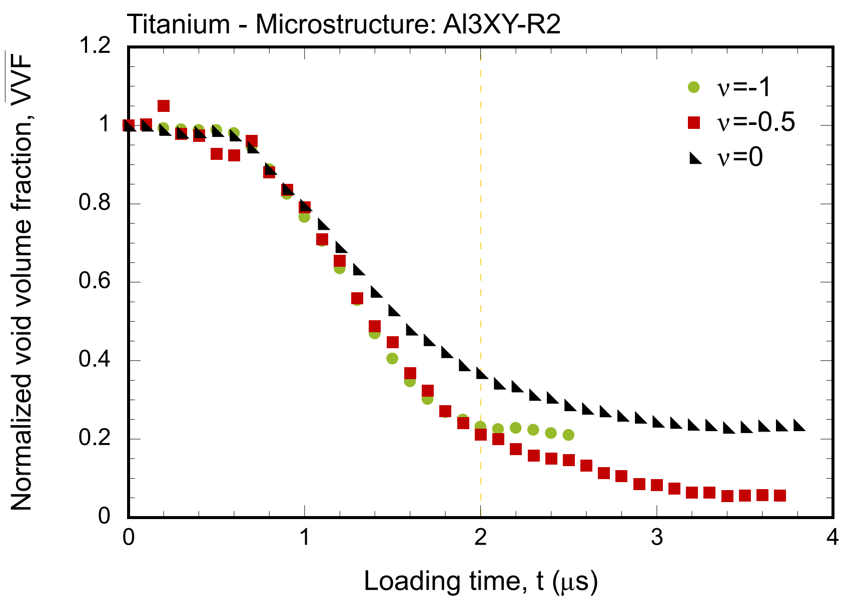

Figure 12: Results corresponding to Titanium with microstructure Al3XY and realization R2. Evolution of the normalized void volume fraction $\overline{VVF} = VVF/VVF_0$ with the loading time t for three different values of the temperature sensitivity exponent: $\nu = –1$, $\nu = –0.5$ and $\nu = 0$ (temperature independent material). The vertical yellow dashed line corresponds to $t = 2$ μs. For interpretation of the references to color in this figure, the reader is referred to the web version of this article.

6. Parametric analysis

This section investigates the main features of the porous microstructure affecting the formation and development of shear bands. Namely, in Section 6.1 we carry out a comparison between calculations performed with three of the microstructures considered in Table 2: SS5XY, Ti0.5XY and INC1XY. Finite element results are shown for both Titanium and CRS 1018 steel, see Table 1. Moreover, Section 6.2 focuses on the effect of initial void volume fraction, and Section 6.3 shows calculations with the same initial void volume fraction but different pore size distributions. The material parameters used in the calculations of Sections 6.2 and 6.3 correspond to Titanium.

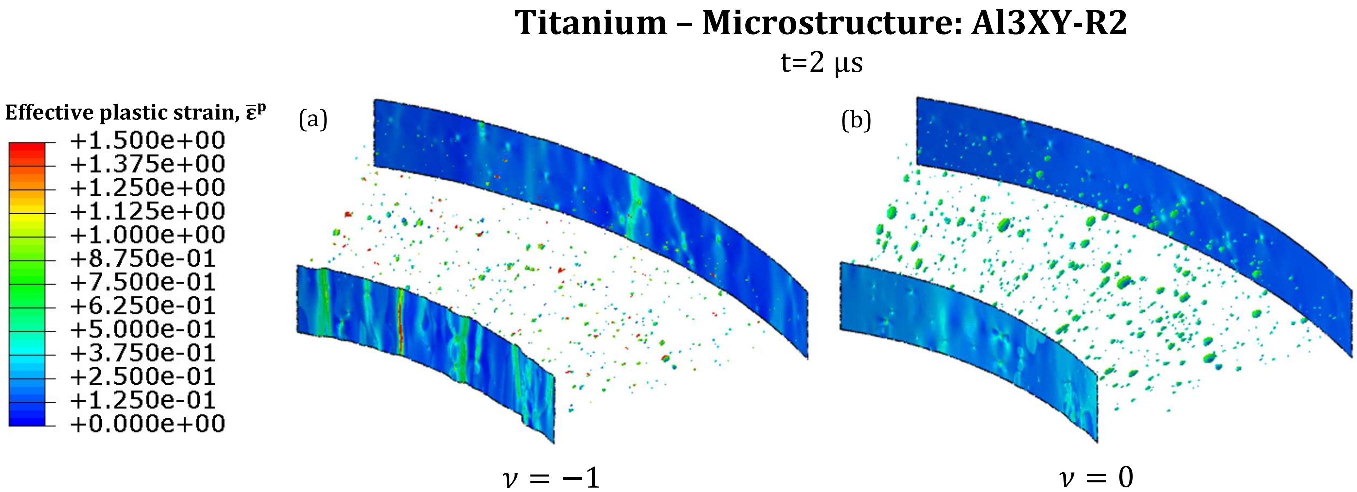

Figure 13: Results corresponding to Titanium with microstructure Al3XY and realization R2. Contours of effective plastic strain $\bar{\varepsilon}^p$ for two different values of the temperature sensitivity exponent: (a) $\nu = -1$ and (b) $\nu = 0$ (temperature independent material). The loading time is $t = 2$ μs.

6.1. The effect of porosity distribution

Fig. 14 shows contours of effective plastic strain for microstructures SS5XY, Ti0.5XY and INC1XY, and realization R1, with material parameters corresponding to Titanium, see Table 1, and for a loading time of 2 μs. The shear bands pattern is more developed for the microstructure INC1XY which displays the greater void volume fraction and contains the bigger voids (the individual effects of void volume fraction and voids size are investigated in Sections 6.2 and 6.3, respectively). For microstructures SS5XY and Ti0.5XY, the gradients of plastic strain in the specimen are smaller (less color contrast), there are less shear bands, and their length is comparatively less, as the plastic strain inside the bands decreases faster as the bands propagate towards the external radius of the sample. For instance, the results for the evolution of the plastic strain along the inner perimeter of the sample reported in Fig. 16(a) show that the number of shear bands (i.e., the number of peaks in the $\bar{\varepsilon}^p - \bar{P}$ curves) is 6, 4 and 7 for SS5XY, Ti0.5XY and INC1XY (the shear bands are indicated with colored arrows), respectively, with the plastic strain in the valleys of the $\bar{\varepsilon}^p - \bar{P}$ curves being smaller in the case of INC1XY, which indicates earlier shear localization. Notice also that for microstructures SS5XY and Ti0.5XY the voids are *all* closed for $t = 2$ μs (no voids are seen in the *empty representations* of the samples included in Fig. 14), while in the case of INC1XY there are pores of various sizes in different zones of the specimen. These results make apparent the role of porous microstructure on the number and the development of the shear bands. Moreover, while the results in Figs. 14 and 16(a) correspond to realization R1, we have checked that the same trends and conclusions are obtained for other realizations of the same microstructures.

Contour plots of effective plastic strain for calculations performed with the material parameters corresponding to CRS 1018 Steel, see Table 1, and the same porous microstructures (SS5XY, Ti0.5XY and INC1XY for realization R1), are pictured in Fig. 15. The loading time is 4 μs. Note that the inner copper cylinder collapses shortly after 4 μs, so that the contour plots nearly show the maximum strain attained in the specimens. The comparison with the results of Fig. 14 shows that the CRS Steel is less prone to shear localization, as no shear bands are observed for microstructures SS5XY and Ti0.5XY, and in the case of INC1XY the shear bands are less developed and shorter. The reason is most likely because CRS 1018 Steel shows less temperature sensitivity than Titanium ($\nu = -0.38$ versus $\nu = -1.7$), see Table 1. Note that the plastic strain field in the specimen for SS5XY and Ti0.5XY is largely homogeneous, such that the plastic strain increases uniformly towards the outer radius, similarly to the results reported in Fig. 10 for the temperature independent material with parameters corresponding to Titanium. In the case of INC1XY, the plastic strain field is more similar to the results reported in Fig. 10 for a material with an intermediate value of the thermal softening exponent $\nu = -0.5$, showing multiple shear bands that propagate a short distance from the inner radius of the specimen before dying out, and displaying a definite resemblance with the experimental observations reported, for instance, in Fig. 5 of Nesterenko et al. (1997). The results for the evolution of the plastic strain along the inner perimeter of the specimen reported in Fig. 16(b) show 12 shear bands for the microstructure INC1XY (i.e., 12 peaks in the $\bar{\varepsilon}^p - \bar{P}$ curve). On the other hand, the plastic localization is not much developed in comparison with the results obtained for the same microstructure and the parameters of Titanium, see Fig. 16(a), as the difference in plastic strain between peaks and valleys is less. Notice also that the $\bar{\varepsilon}^p - \bar{P}$ curves for SS5XY and Ti0.5XY in Fig. 16(b) do not show a succession of peaks and valleys as no shear bands are formed, unlike in the case of Fig. 16(a) for the calculations carried out with the parameters of Titanium. The finite element results reported in this section make apparent the influence of the material response on the formation and development of shear bands in porous metals.

6.2. The effect of void volume fraction

The material behavior is modeled with the parameters corresponding to Titanium, see Table 1. Using the microstructure Al3XY-R1 as a reference porosity distribution, we randomly remove some voids until two initial void volume fractions, namely $VVF_0 = 0.5\%$ and 0.1%, are reached (recall that the initial void volume fraction for the microstructure Al3XY is 2.17%, see Table 2). The voids deletion process to obtain the two initial volume fractions is performed independently, i.e., we do not generate the porosity distribution with $VVF_0 = 0.1\%$ from the one with 0.5%, instead they both derive directly from the parent microstructure with 2.17%.

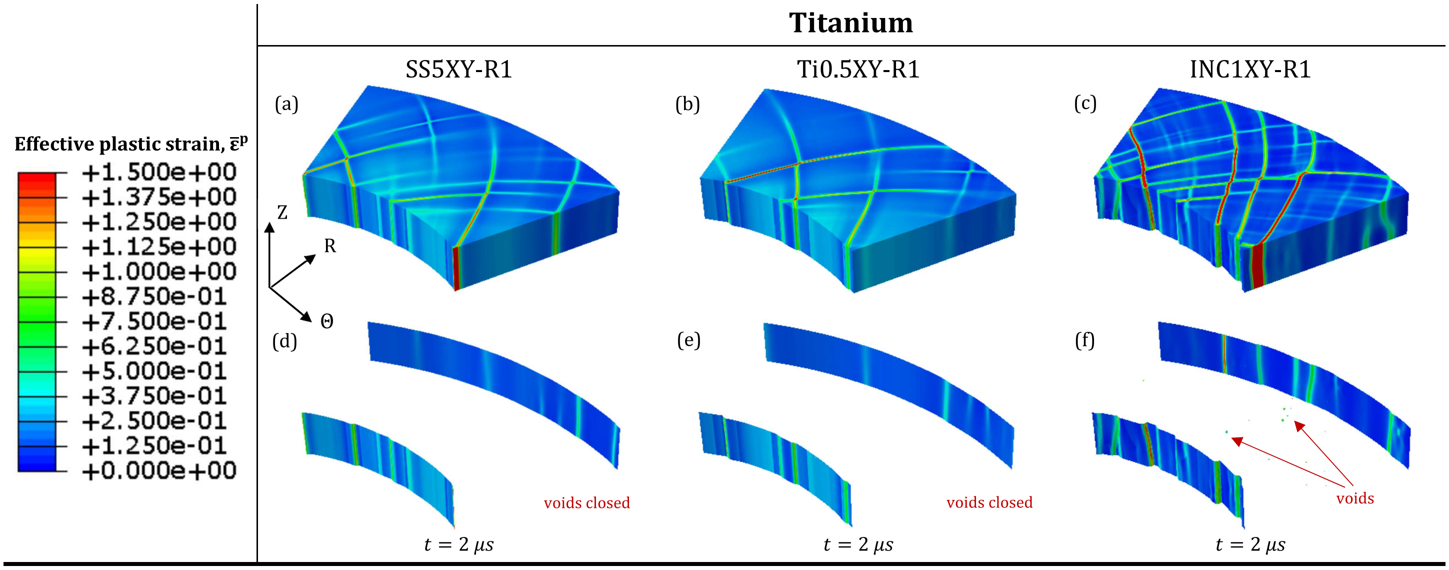

Figure 14: Results corresponding to Titanium. Contours of effective plastic strain $\bar{\varepsilon}^p$ for three different microstructures: (a)-(d) SS5XY, (b)-(e) Ti0.5XY and (c)-(f) INC1XY. The loading time is $t = 2\ \mu$s.

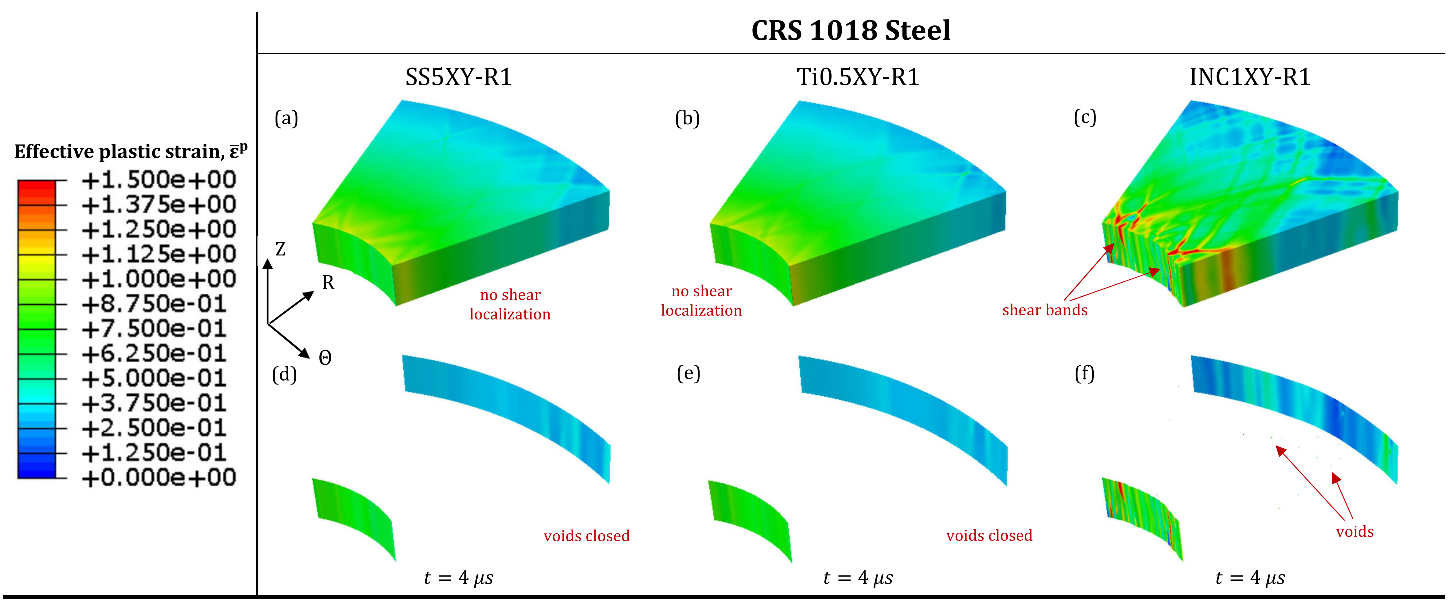

Figure 15: Results corresponding to CRS 1018 steel. Contours of effective plastic strain $\bar{\varepsilon}^p$ for three different microstructures: (a)-(d) SS5XY, (b)-(e) Ti0.5XY and (c)-(f) INC1XY. The loading time is $t = 4\ \mu$s.

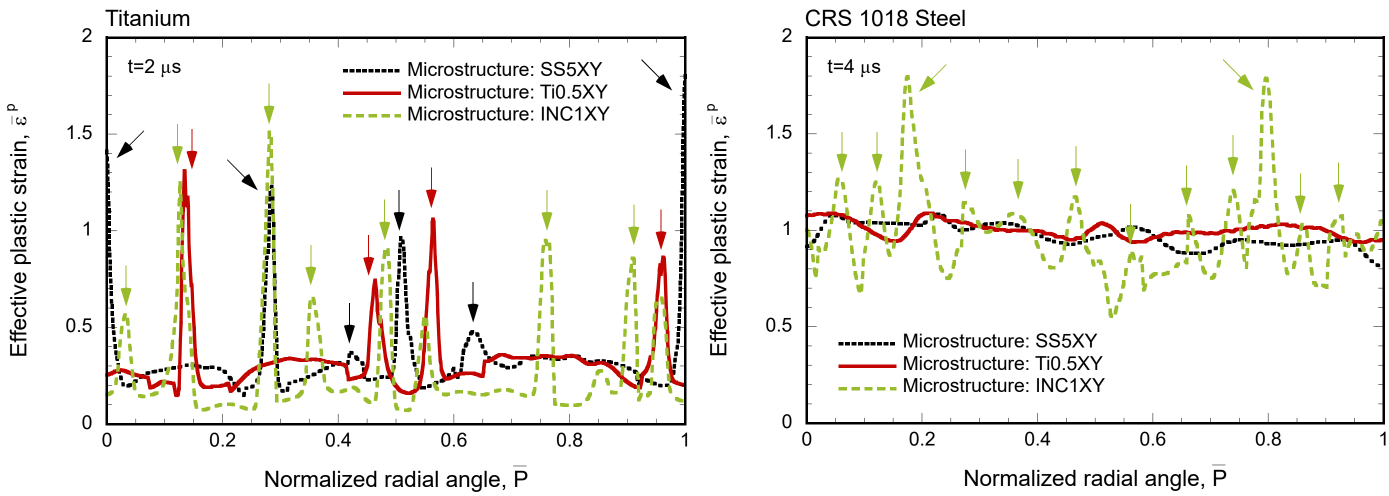

(a) (b)

Figure 16: Results corresponding to three microstructures SS5XY, Ti0.5XY and INC1XY and realization R1. Effective plastic strain $\bar{\varepsilon}^p$ versus normalized inner perimeter of the ring $\bar{P} = \frac{4\theta}{\pi}$ for material parameters corresponding to: (a) Titanium for a loading time of $t = 2$ μs and (b) CRS 1018 steel for a loading time of $t = 4$ μs. The colored arrows indicate the shear bands: black for SS5XY, red for Ti0.5XY and green for INC1XY. For interpretation of the references to color in this figure, the reader is referred to the web version of this article.

Fig. 17 shows contours of effective plastic strain for a loading time of 2 μs, for two calculations with initial void volume fraction 0.1% and 0.5%, respectively. The shear localization patterns for both values of VVF_0 are qualitatively similar, and they also find resemblance with the plastic strain contours of Fig. 4(d) corresponding to the parent microstructure. The quantitative differences in the plastic strain contours shown in Figs. 17(a) and 17(c) are most likely due to the different spatial and size distribution of voids for $VVF_0 = 0.1\%$ and 0.5%. The location and development of the shear bands depends on the initial void volume fraction, so that the results shown in Fig. 18 suggest that increasing the value of VVF_0 favors localization, as the maximum plastic strain is slightly greater for 0.5% than for 0.1% (blue arrows in Fig. 18 indicate the strain excursions with the maximum value of $\bar{\varepsilon}^p$). The same trend is obtained when the $\bar{\varepsilon}^p - \bar{P}$ curves of Fig. 18 are compared with the results reported in Fig. 5(a) for the parent microstructure with $VVF_0 = 2.17\%$, for which the maximum value of the effective plastic strain reaches ≈ 2. Nevertheless, the quantitative differences are not large, as increasing the initial void volume fraction ≈ 20 times, leads to an increase of the maximum value of the effective plastic strain in the inner radius of the specimen of $\approx 25\%$ for the loading time of 2 μs. Moreover, Fig. 19 shows that the temporal evolution of the normalized void volume fraction $\overline{VVF}$ is also similar for the two initial void volume fractions considered. The quantitative differences between the results obtained for 0.1% and 0.5% only appear for $t > 1.5$ μs, after the shear bands pattern is formed, so that the normalized void volume fraction in the specimen when the load is over is greater for 0.1% (while the remaining total void volume fraction is greater for 0.5%, compare the contour plots of Figs. 17(b) and 17(d)). We have also checked that the temporal evolution of $\overline{VVF}$ obtained for the parent microstructure with $VVF_0 = 2.17\%$ is very similar to the results obtained for 0.5% and 0.1% (in fact, the curves for 2.17% and 0.5% practically overlap during the whole loading process, compare Figs. 8 and 19).

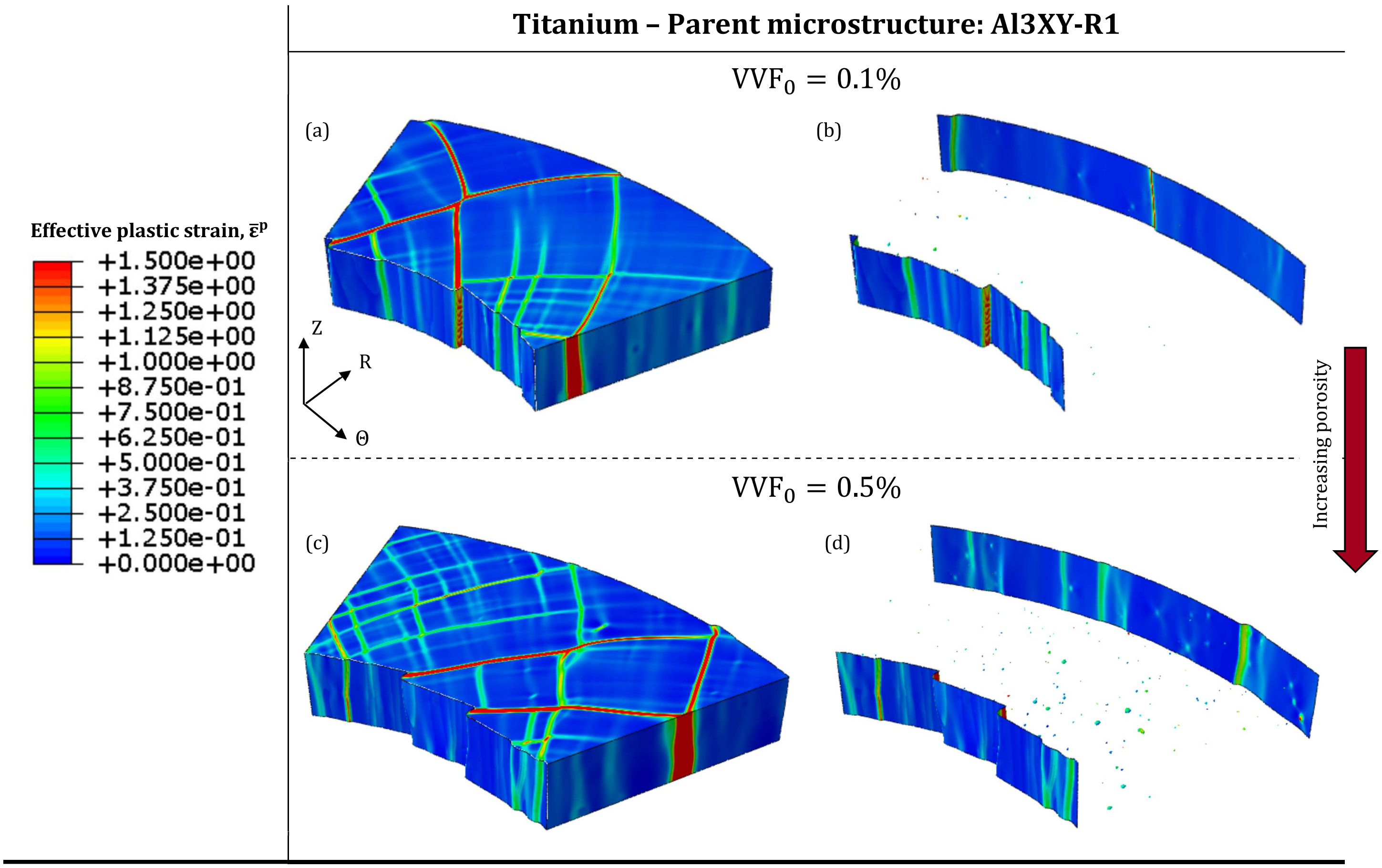

Figure 17: Results corresponding to Titanium with parent microstructure Al3XY and realization R1. Contours of effective plastic strain $\bar{\varepsilon}^p$ for two different values of the initial void volume fraction: (a)-(b) $VVF_0 = 0.1\%$ and (c)-(d) $VVF_0 = 0.5\%$. The loading time is $t = 2$ μs.

6.3. The effect of voids size

As in Section 6.2, the material behavior is modeled with the parameters corresponding to Titanium, see Table 1. Using the Log-normal statistical function fitted to the microstructure Al3XY, see Table 2, we generate additional porous microstructures alternately varying the mean and the standard deviation of the Log-normal distribution, but keeping constant the initial void volume fraction, i.e., $VVF_0 = 2.17\%$ in all the calculations presented in this section.

Fig. 20 displays contours of effective plastic strain for two different values of the voids mean diameter, $\mu = 10$ μm

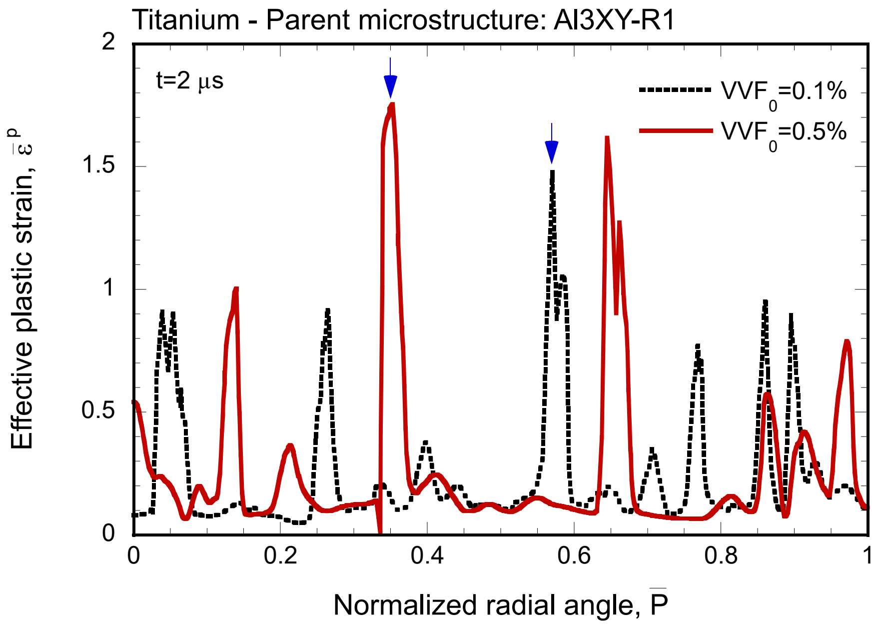

Figure 18: Results corresponding to Titanium with parent microstructure Al3XY and realization R1. Effective plastic strain $\bar{\varepsilon}^p$ versus normalized inner perimeter of the ring $\bar{P} = \frac{4\theta}{\pi}$ for two different values of the initial void volume fraction $VVF_0 = 0.1\%$ and 0.5%. The loading time is $t = 2$ μs. The blue arrows indicate the strain excursions with the maximum value of effective plastic strain. For interpretation of the references to color in this figure, the reader is referred to the web version of this article.

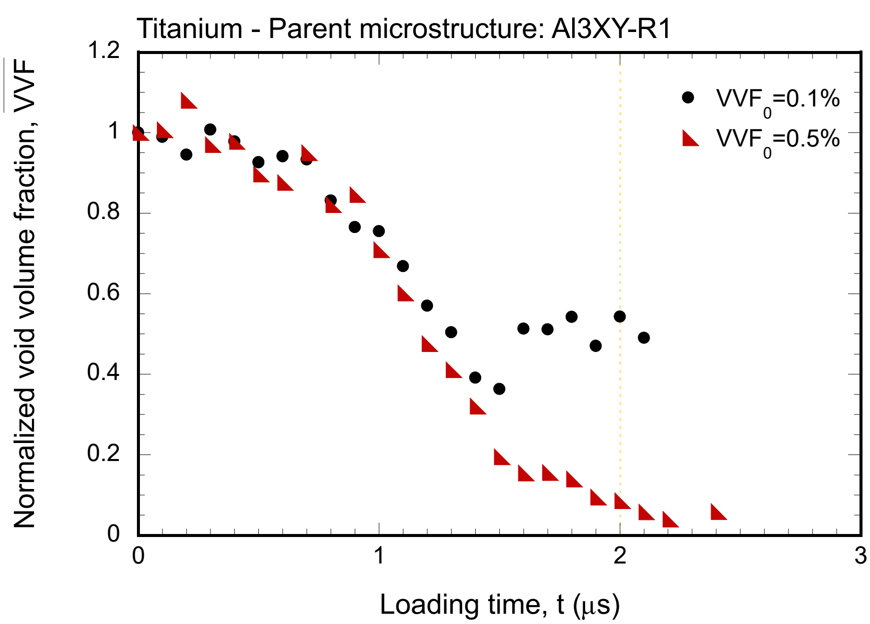

Figure 19: Results corresponding to Titanium with parent microstructure Al3XY and realization R1. Evolution of the normalized void volume fraction $\overline{VVF} = VVF/VVF_0$ with the loading time t for two different values of the initial void volume fraction $VVF_0 = 0.1\%$ and 0.5%. The vertical yellow dashed line corresponds to $t = 2$ μs. For interpretation of the references to color in this figure, the reader is referred to the web version of this article.

and $\mu = 30$ μm, keeping the standard deviation of the distribution of void sizes the same (in % of the mean voids size), for three different loading times (in order to illustrate the process of shear localization). Note that, as the initial void volume fraction is the same, decreasing/increasing the mean size of the voids while keeping constant the standard deviation of the distribution of void sizes, implies to increase/decrease the number of pores. Specifically, for $\mu = 10$ μm there are more voids and they are smaller than for $\mu = 30$ μm (compare Figs. 20(d) and 20(j)). The contour plots show that more shear bands are nucleated in the case of $\mu = 10$ μm, but they are comparatively less developed than in the case of $\mu = 30$ μm (compare Figs. 20(c) and 20(i)). Namely, the results for the evolution of the plastic strain along the inner radius of the specimen reported in Fig. 21 show that the number of shear bands is 6 and 11 for the microstructures with mean voids diameter of 30 μm and 10 μm, respectively, and that larger values of plastic strain inside the bands are attained for the microstructure with mean voids diameter of 30 μm. The greater development of the shear bands is related to fact that shear localization occurs earlier for the microstructure which contains greater voids (compare Figs. 20(b) and 20(h)). In fact, the temporal evolution of the normalized void volume fraction $\overline{VVF}$ pictured in Fig. 22 shows that the rate of collapse of the voids occurs faster for the microstructure with $\mu = 30$ μm, which is an indicator of plastic localization occurring more rapidly (see the results reported for materials with different temperature sensitivities in Fig. 12 and the discussion therein).

Fig. 23 shows contours of effective plastic strain for two different values of the standard deviation of the Log-normal function used to generate the porous microstructure, $dev = 1.5$ μm ($\approx 10\%$ of the mean voids size) and $dev = 10$ μm ($\approx 60\%$ of the mean voids size). The mean voids diameter for the distributions with $dev = 1.5$ μm and $dev = 10$ μm is the same, $\mu = 15.98$ μm, see Table 2. The results correspond to three different loading times, $t = 1$ μs, 1.5 μs and 2 μs. As the initial void volume fraction and the mean voids diameter are fixed, increasing the standard deviation of the voids size distribution implies that the porous microstructure contains greater voids (also smaller), as depicted in Figs. 23(d) and 23(j), promoting early shear localization (compare of Figs. 23(a)-(b) and 23(g)-(h)) and leading to a more rapid decrease of the material porosity during loading (see Fig. 24), consistent with the results obtained above increasing the mean size of the voids. Similarly, increasing the standard deviation of the voids size distribution also favors the development of the shear bands, so that for a loading time of 2 μs, the plastic strain inside the localization bands reaches greater values for $dev = 10$ μm than for $dev = 1.5$ μm, see Fig. 25. In contrast, the number of shear bands is inversely related to the standard deviation of the pore sizes distribution, as shown in Fig. 25, where 13 shear bands are identified for $dev = 1.5$ μm and 9 for $dev = 10$ μm, reinforcing the idea that for a microstructure containing bigger pores, the number of shear bands is less. Note that

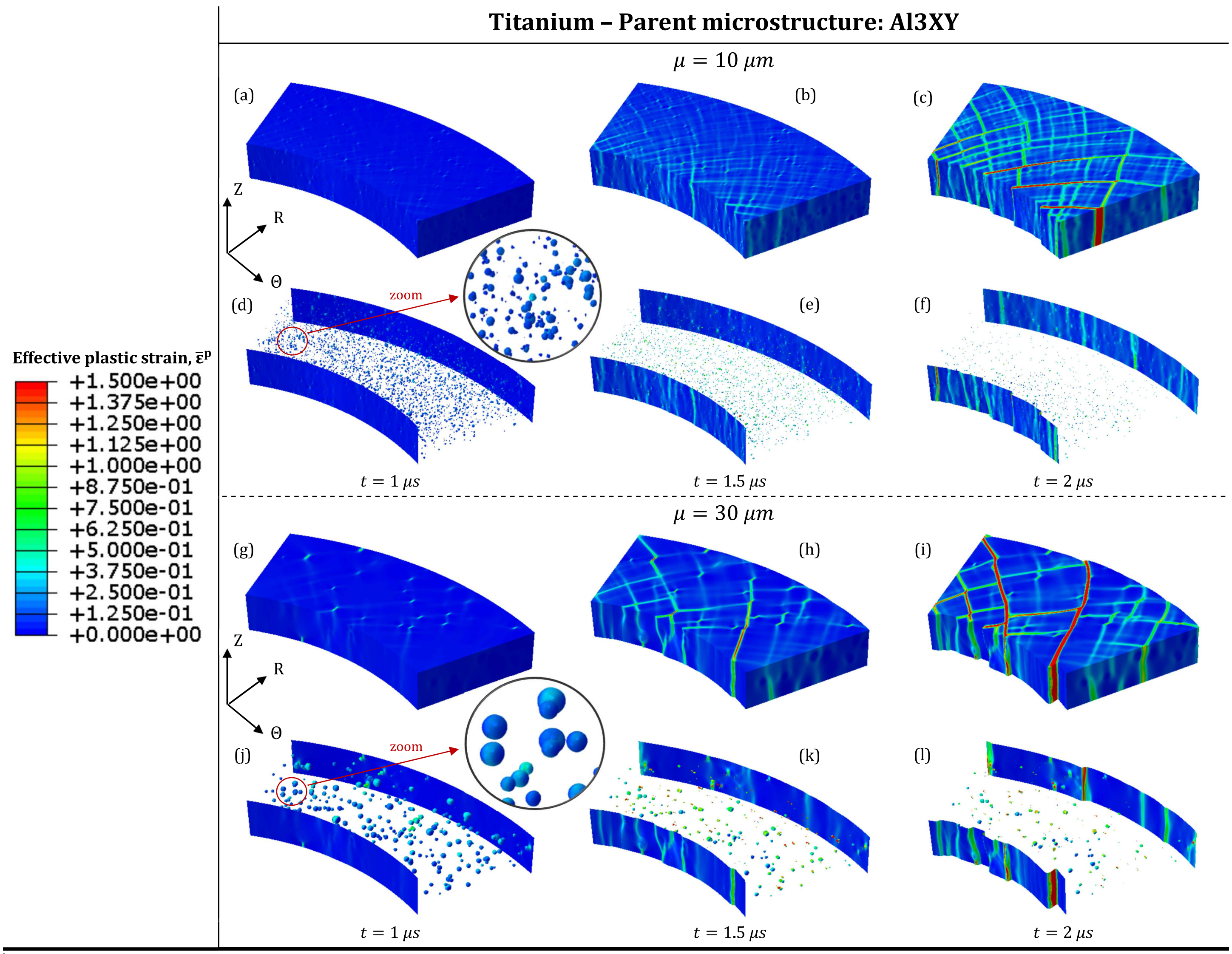

Figure 20: Results corresponding to Titanium with parent microstructure Al3XY. Contours of effective plastic strain $\bar{\varepsilon}^p$ for two different values of the voids mean size: $\mu = 10$ μm for different loading times (a)-(d) $t = 1$ μs, (b)-(e) $t = 1.5$ μs, (c)-(f) $t = 2$ μs, and $\mu = 30$ μm for different loading times (g)-(j) $t = 1$ μs, (h)-(k) $t = 1.5$ μs, (i)-(l) $t = 2$ μs. Subplots (a)-(b)-(c)-(g)-(h)-(i) correspond to *solid representations* of the specimen which show the formation and development of multiple shear bands. Subplots (d)-(e)-(f)-(j)-(k)-(l) correspond to *empty representations* of the specimen which show the evolution of the porous microstructure.

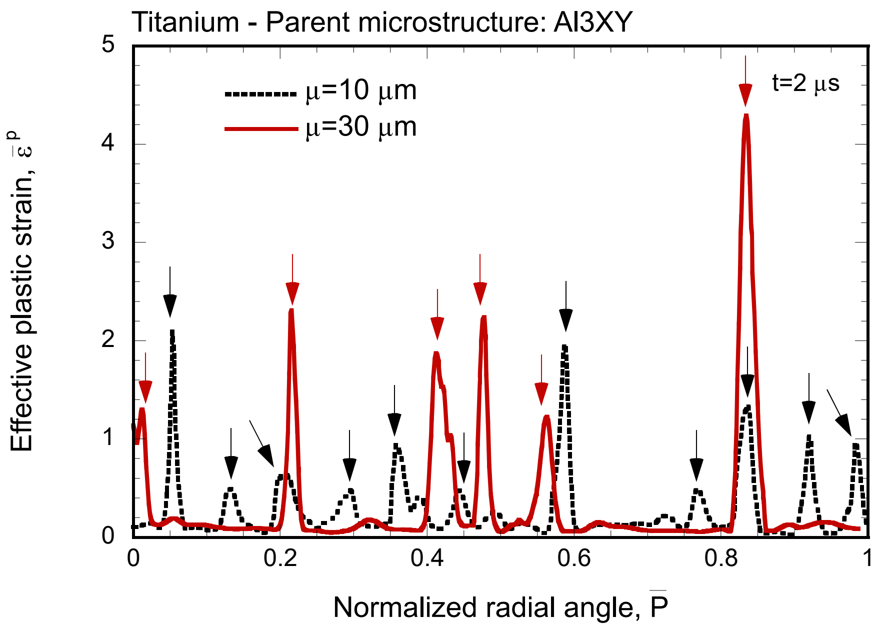

Figure 21: Results corresponding to Titanium with parent microstructure Al3XY. Effective plastic strain $\bar{\varepsilon}^p$ versus normalized inner perimeter of the ring $\bar{P} = \frac{4\theta}{\pi}$ for two different values of the voids mean size $\mu = 10$ μm and $\mu = 30$ μm. The loading time is $t = 2$ μs. The colored arrows indicate the shear bands: black for $\mu = 10$ μm and red for $\mu = 30$ μm. For interpretation of the references to color in this figure, the reader is referred to the web version of this article.

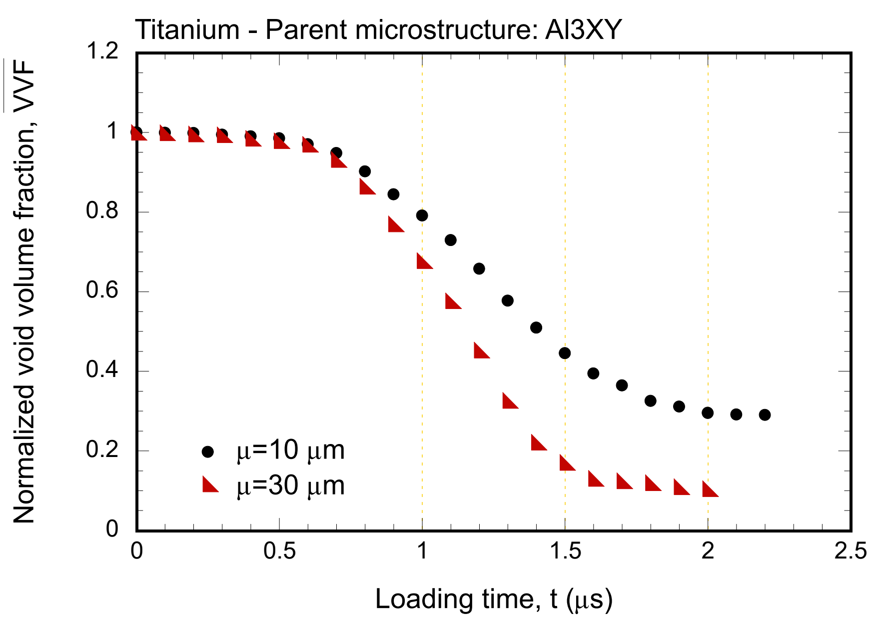

Figure 22: Results corresponding to Titanium with parent microstructure Al3XY. Evolution of the normalized void volume fraction $\overline{VVF} = VVF/VVF_0$ with the loading time t for two different values of the voids mean size $\mu = 10$ μm and $\mu = 30$ μm. The vertical yellow dashed lines correspond to $t = 1$ μs, 1.5 μs, 2 μs. For interpretation of the references to color in this figure, the reader is referred to the web version of this article.

the influence of voids size distribution on shear bands formation cannot be captured in finite element simulations which describe the material behavior with standard constitutive models where the porosity stands for a single internal variable with no contribution of the void size.

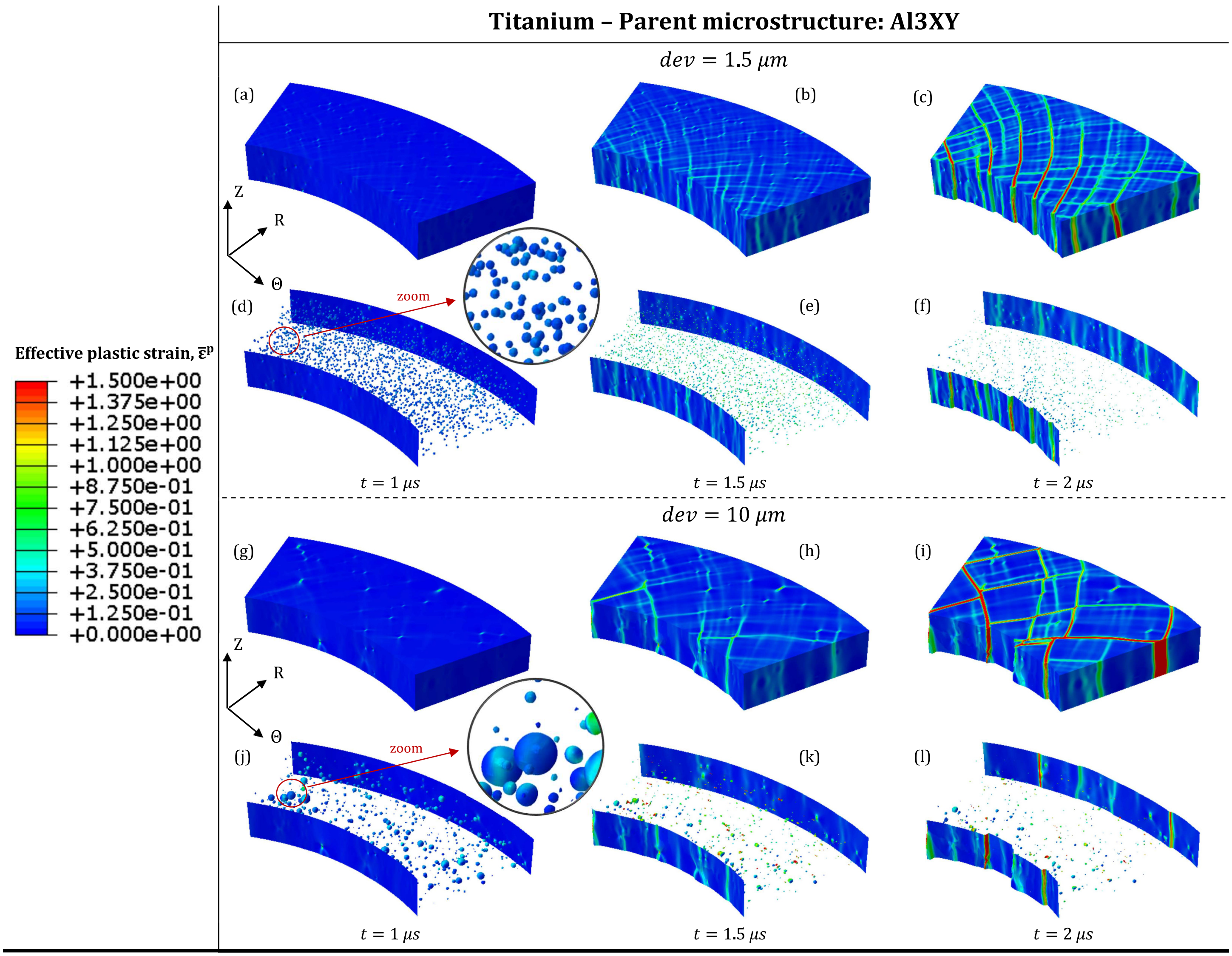

Figure 23: Results corresponding to Titanium with parent microstructure Al3XY. Contours of effective plastic strain $\bar{\varepsilon}^p$ for two different values of the standard deviation: $dev = 1.5\ \mu$m for different loading times (a)-(d) $t = 1\ \mu$s, (b)-(e) $t = 1\ \mu$s, (c)-(f) $t = 2\ \mu$s, and $dev = 10\ \mu$m for different loading times (g)-(j) $t = 1\ \mu$s, (h)-(k) $t = 1.5\ \mu$s, (i)-(l) $t = 2\ \mu$s. Subplots (a)-(b)-(c)-(g)-(h)-(i) correspond to *solid representations* of the specimen which show the formation and development of multiple shear bands. Subplots (d)-(e)-(f)-(j)-(k)-(l) correspond to *empty representations* of the specimen with the evolution of the porous microstructure.

7. Concluding remarks

In this paper, we have investigated using finite element simulations the effect of microstructural porosity on the formation of multiple shear bands in thick-walled cylinders subjected to rapid radial collapse. For that purpose, we

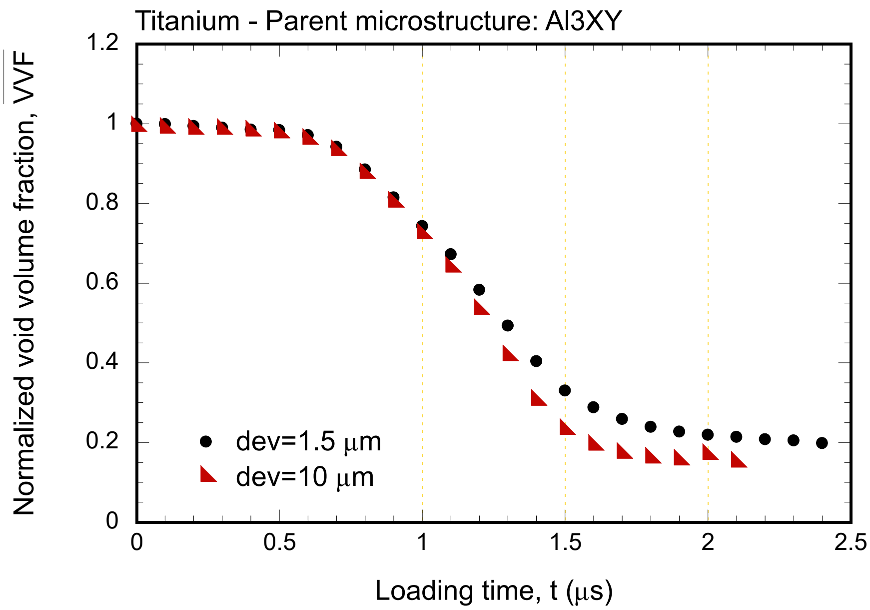

Figure 24: Results corresponding to Titanium with parent microstructure Al3XY. Evolution of the normalized void volume fraction $\overline{VVF} = VVF/VVF_0$ with the loading time t for two different values of the standard deviation, $dev = 1.5$ μm and $dev = 10$ μm. The vertical yellow dashed lines correspond to $t = 1$ μs, 1.5 μs, 2 μs. For interpretation of the references to color in this figure, the reader is referred to the web version of this article.

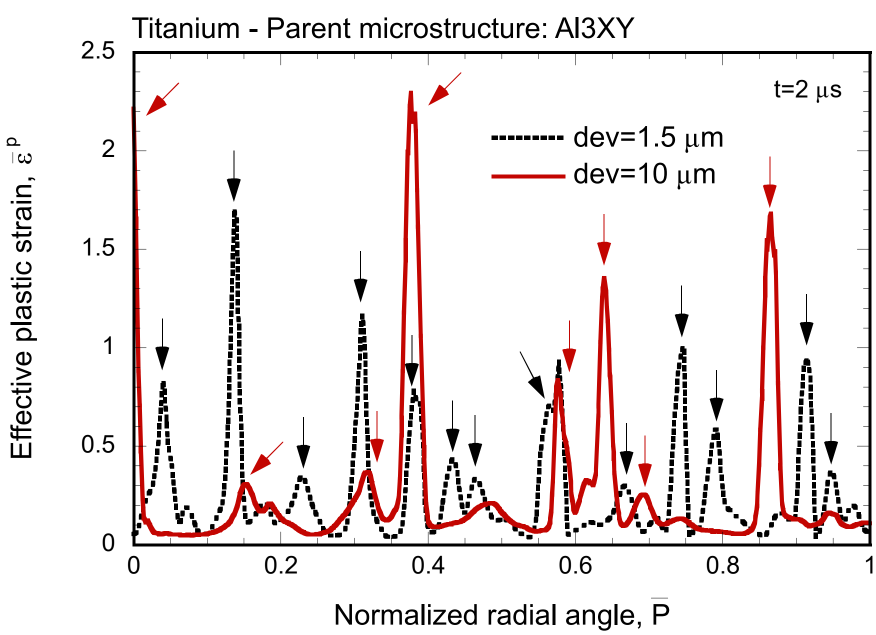

Figure 25: Results corresponding to Titanium with parent microstructure Al3XY. Effective plastic strain $\bar{\varepsilon}^p$ versus normalized inner perimeter of the ring $\bar{P} = \frac{4\theta}{\pi}$ for two different values of the standard deviation, $dev = 1.5$ μm and $dev = 10$ μm. The loading time is $t = 2$ μs. The colored arrows indicate the shear bands: black for $dev = 1.5$ μm and red for $dev = 10$ μm. For interpretation of the references to color in this figure, the reader is referred to the web version of this article.

have used the methodology developed by Marvi-Mashhadi et al. (2021) to incorporate into the finite element model the porosity distributions corresponding to 4 additively manufactured metals for which the void volume fraction ranges between $\approx 0.001\%$ and $\approx 2\%$, and the size of the pores varies from ≈ 6 μm to ≈ 110 μm. For each of the 4 porous microstructures considered, we have created three realizations in order to take into account the scatter in the finite element results caused by the random spatial distribution of pores. To the authors' knowledge, these are the first calculations ever performed to study the effect of porosity on dynamic shear localization which include the actual representation of voids in the specimen. The mechanical behavior of the material is modeled as elastic-plastic, with yielding described by the von Mises criterion, an associated flow rule and a thermo-viscoplastic constitutive relation for the evolution of the yield stress. Two sets of material parameters corresponding to Titanium and CRS 1018 Steel have been used in the calculations. The key conclusions of this work are as follows:

- Microstructural porosity favors the formation and development of shear bands in temperature softening materials.

- For temperature independent materials, microstructural porosity alone does not trigger the formation of shear bands.

- Thermal softening is essential for the shear bands to form in porous materials, and the greater the thermal softening, the earlier the shear localization and the faster the shear bands propagation.

- The increase of the void volume fraction shows a moderate effect on the shear localization process, the maximum diameter of the pores being the main microstructural feature affecting the shear localization process.

- Increasing the maximum diameter of the voids favors early shear localization and decreases the number of shear bands.

- For a given void volume fraction, increasing the number of pores increases the number of shear bands.

- Realizations with different spatial distribution of voids corresponding to the same porous microstructure lead to the formation of similar number of shear bands.

Altogether, this work brings new insights into the effect of porosity on adiabatic shear banding, and establishes a novel methodological framework to assess the performance of porous ductile materials –like additive manufactured metals– under dynamic shearing. On the other hand, additional efforts are needed to increase the generality of the conclusions obtained in this work, that should be substantiated for other shear dominated impact problems and different material behaviors. Moreover, calculations for different loading rates should be performed in future works to investigate the interplay between material porosity and inertia on the shear bands patterns.

Acknowledgements

The authors acknowledge the fruitful discussions on adiabatic shear localization with Professor Alain Molinari (University of Lorraine, Metz), Professor Daniel Rittel (Technion, Haifa) and Dr. Zev Lovinger (Rafael).

Funding

The research leading to these results has received funding from the European Research Council (ERC) under the European Union's Horizon 2020 research and innovation programme. Project PURPOSE, grant agreement 758056.

Conflict of interest

The authors declare that they have no conflict of interest.

Author contributions

A. R. Vishnu: Conceptualization; Data curation; Formal analysis; Investigation; Software; Validation; Writing - original draft; Writing - review & editing. **M. Marvi-Mashhadi**: Conceptualization; Methodology; Software; Supervision; Writing - review & editing. **J. C. Nieto-Fuentes**: Conceptualization; Investigation; Methodology; Software; Supervision; Writing - review & editing. **J. A. Rodríguez-Martínez**: Conceptualization; Formal analysis; Funding acquisition; Investigation; Methodology; Project administration; Resources; Supervision; Validation; Visualization; Writing - original draft; Writing - review & editing.

References

ABAQUS/Explicit, 2016. Abaqus Explicit v6.16 User's Manual. version 6.16 ed., ABAQUS Inc., Richmond, USA.

Alkhader, M., Bodelot, L., 2011. Large strain mechanical behavior of HSLA-100 Steel over a wide range of strain rates. Journal of Engineering Materials and Technology 134.

Andrade, U., Meyers, M.A., Vecchio, K.S., Chokshi, A.H., 1994. Dynamic recrystallization in high-strain, high-strain-rate plastic deformation of copper. Acta Metallurgica et Materialia 42, 3183–95.

Areias, P.M.A., Belytschko, T., 2007. Two-scale method for shear bands: thermal effects and variable bandwidth. International Journal for Numerical Methods in Engineering 72, 658–96.

Bai, Y., Xuc, Q., Xu, Y., Shen, L., 1994. Characteristics and microstructure in the evolution of shear localization in Ti-6A1-4V alloy. Mechanics of Materials 17, 155–64.

Bargieł, M., Mościński, J., 1991. C-language program for the irregular close packing of hard spheres. Computer Physics Communications 64, 183–92.

Becker, R., 2017. Direct numerical simulation of ductile spall failure. International Journal of Fracture 208, 5–26.

Becker, R., Callaghan, K., 2020. Void growth dependence on loading path and mean stress from large-scale numerical simulations. International Journal of Plasticity 134, 102780.

Bondar, M.P., Nesterenko, V.F., 1991. Strain correlation at different structural levels for dynamically loaded hollow copper cylinders. Le Journal de Physique IV 1, C3–163.

Bonnet-Lebouvier, A.S., Molinari, A., Lipinski, P., 2002. Analysis of the dynamic propagation of adiabatic shear bands. International Journal of Solids and Structures 39, 4249–69.

Børvik, T., Leinum, J.R., Solberg, J.K., Hopperstad, O.S., Langseth, M., 2001. Observations on shear plug formation in Weldox 460 E steel plates impacted by blunt-nosed projectiles. International Journal of Impact Engineering 25, 553–72.

Bronkhorst, C.A., Cerreta, E.K., Xue, Q., Maudlin, P.J., Mason, T.A., Gray, G.T., 2006. An experimental and numerical study of the localization behavior of tantalum and stainless steel. International Journal of Plasticity 22, 1304–35.

Burns, T.J., Davies, M.A., 2002. On repeated adiabatic shear band formation during high-speed machining. International Journal of Plasticity 18, 487–506.

Campbell, J.D., Ferguson, W.G., 1970. The temperature and strain-rate dependence of the shear strength of mild steel. The Philosophical Magazine: A Journal of Theoretical Experimental and Applied Physics 21, 63–82.

Dao, M., Li, M., 2001. A micromechanics study on strain-localization-induced fracture initiation in bending using crystal plasticity models. Philosophical Magazine A 81, 1997–2020.

Dodd, B., Atkins, A.G., 1983. Flow localization in shear deformation of void-containing and void-free solids. Acta Metallurgica 31, 9–15.

Dorogoy, A., Rittel, D., Godinger, A., 2015. Modification of the shear-compression specimen for large strain testing. Experimental Mechanics 55, 1627–39.

Dorothy, H.L., Longère, P., 2019. Unified modelling of adiabatic shear banding and subsequent micro-voiding driven dynamic failure of viscoplastic solids. International Journal of Impact Engineering 132, 103322.

Duffy, J., Chi, Y., 1992. On the measurement of local strain and temperature during the formation of adiabatic shear bands. Materials Science and Engineering: A 157, 195–210.

Edwards, N.J., Song, W., Cimpoeru, S.J., Ruan, D., Lu, G., Herzig, N., 2018. Mechanical and microstructural properties of 2024-T351 aluminium using a hat-shaped specimen at high strain rates. Materials Science and Engineering: A 720, 203–13.

Ferguson, W.G., Hauser, F.E., Dorn, J.E., 1967. Dislocation damping in zinc single crystals. British Journal of Applied Physics 18, 411–7.

Gaudillière, C., Ranc, N., Larue, A., Lorong, P., 2010. Investigations in high speed blanking: cutting forces and microscopic observations. EPJ Web of Conferences 6, 19003.

Gil Sevillano, J., Van Houtte, P., Aernoudt, E., 1977. The contribution of macroscopic shear bands to the rolling texture of FCC metals. Scripta Metallurgica 11, 581–5.

Gu, Y., Ravichandran, G., 2005. Prediction of incipient shear band trajectories in a thick wall cylinder explosion test. Experimental Mechanics 45, 447–50.

Guduru, P.R., Freund, L.B., 2002. The dynamics of multiple neck formation and fragmentation in high rate extension of ductile materials. International Journal of Solids and Structures 39, 5615–32.

Guo, Y., Li, Y., 2012. A novel approach to testing the dynamic shear response of Ti-6Al-4V. Acta Mechanica Solida Sinica 25, 299–311.

Gurson, A.L., 1977. Continuum theory of ductile rupture by void nucleation and growth. Part I: Yield criteria and flow rules for porous ductile media. ASME Journal of Engineering Materials and Technology 99, 2–15.

Hartley, K.A., Duffy, J., Hawley, R.H., 1987. Measurement of the temperature profile during shear band formation in steels deforming at high strain rates. Journal of the Mechanics and Physics of Solids 35, 283–301.

Johnson, G.R., Cook, W.H., 1983. A constitutive model and data for materials subjected to large strains, high strain rates, and high temperatures. Proceedings of the 7th International Symposium on Ballistics , 541–7.

Klepaczko, J.R., 1994. An experimental technique for shear testing at high and very high strain rates. The case of a mild steel. International Journal of Impact Engineering 15, 25–39.

Kubair, D.V., Ramesh, K.T., Swaminathan, P.K., 2015. Effect of shear-void-growth-softening on adiabatic shear-band-spacing in ductile materials. Acta Mechanica 226, 4189–206.

Kuroda, M., Needleman, A., 2019. Nonuniform and localized deformation in single crystals under dynamic tensile loading. Journal of the Mechanics and Physics of Solids 125, 347–59.

Kuroda, M., Tvergaard, V., 2007. Effects of texture on shear band formation in plane strain tension/compression and bending. International Journal of Plasticity 23, 244–72.

Landau, P., Osovski, S., Venkert, A., Gärtnerová, V., Rittel, D., 2016. The genesis of adiabatic shear bands. Scientific reports 6, 1–6.

Lieou, C.K.C., Bronkhorst, C.A., 2018. Dynamic recrystallization in adiabatic shear banding: Effective-temperature model and comparison to experiments in ultrafine-grained titanium. International Journal of Plasticity 111, 107–21.

Lieou, C.K.C., Mourad, H.M., Bronkhorst, C.A., 2019. Strain localization and dynamic recrystallization in polycrystalline metals: thermodynamic theory and simulation framework. International Journal of Plasticity 119, 171–87.

Lins, J.F.C., Sandim, H.R.Z., Kestenbach, H.J., Raabe, D., Vecchio, K.S., 2007. A microstructural investigation of adiabatic shear bands in an interstitial free steel. Materials Science and Engineering: A 457, 205–18.

Liu, M., Guo, Z., Fan, C., Tang, T., Wang, X., Hu, H., 2016. Modeling spontaneous shear bands evolution in thick-walled cylinders subjected to external high-strain-rate loading. International Journal of Solids and Structures 97–98, 336–54.

Longère, P., Dragon, A., 2016. Enlarged finite strain modelling incorporating adiabatic shear banding and post-localization microvoiding as shear failure mechanisms. International Journal of Damage Mechanics 25, 1142–69.

Lovinger, Z., Rikanati, A., Rosenberg, Z., Rittel, D., 2011. Eletro-magnetic collapse of thick-walled cylinders to investigate spontaneous shear localization. International Journal of Impact Engineering 38, 918–29.

Lovinger, Z., Rittel, D., Rosenberg, Z., 2015. An experimental study on spontaneous adiabatic shear band formation in electro-magnetically collapsing cylinders. Journal of the Mechanics and Physics of Solids 79, 134–56.

Lovinger, Z., Rittel, D., Rosenberg, Z., 2018. Modeling spontaneous adiabatic shear band formation in electro-magnetically collapsing thick-walled cylinders. Mechanics of Materials 116, 130–45. IUTAM Symposium on Dynamic Instabilities in Solids.

Magagnosc, D.J., Lloyd, J.T., Meredith, C.S., Pilchak, A.L., Schuster, B.E., 2021. Incipient dynamic recrystallization and adiabatic shear bands in Ti–7Al studied via in situ X-ray diffraction. International Journal of Plasticity 141, 102992.

Marchand, A., Duffy, J., 1988. An experimental study of the formation process of adiabatic shear bands in a structural steel. Journal of the Mechanics and Physics of Solids 36, 251–83.

Marvi-Mashhadi, M., Vaz-Romero, A., Sket, F., Rodríguez-Martínez, J.A., 2021. Finite element analysis to determine the role of porosity in dynamic localization and fragmentation: Application to porous microstructures obtained from additively manufactured materials. International Journal of Plasticity 143, 102999.

Mathur, P.S., Backofen, W.A., 1973. Mechanical contributions to the plane-strain deformation and recrystallization textures of aluminum-killed steel. Metallurgical Transactions 4, 643–51.

Meyer, L.W., Manwaring, S., 1985. Critical adiabatic shear strength of low alloyed steel under compressive loading, in: International Conference on Metallurgical Applications of Shock-Wave and High-Strain-Rate Phenomena EXPLOMET85, pp. 657–74.

Meyers, M.A., Chen, Y.J., Marquis, F.D.S., Kim, D.S., 1995. High-strain, high-strain-rate behavior of tantalum. Metallurgical and Materials Transactions A 26, 2493–501.

Mises, R.V., 1928. Mechanik der plastischen formänderung von kristallen. ZAMM - Journal of Applied Mathematics and Mechanics / Zeitschrift für Angewandte Mathematik und Mechanik 8, 161–85.

Molinari, A., 1991. Shear band analysis, in: Non Linear Phenomena in Materials Science I, Trans Tech Publications Ltd. pp. 447–67.

Molinari, A., 1997. Collective behaviour and spacing of adiabatic shear bands. Journal of the Mechanics and Physics of Solids 45, 1551–75.

Molinari, A., Clifton, R.J., 1987. Analytical characterization of shear localization in themoviscoplastic materials. Journal of Applied Mechanics 54, 806–12.

Molinari, A., Musquar, C., Sutter, G., 2002. Adiabatic shear banding in high speed machining of Ti-6Al-4V: Experiments and modeling. International Journal of Plasticity 18, 443–59.

Mourad, H.M., Bronkhorst, C.A., Livescu, V., Plohr, J., Cerreta, E.K., 2017. Modeling and simulation framework for dynamic strain localization in elasto-viscoplastic metallic materials subject to large deformations. International Journal of Plasticity 88, 1–26.

Nahshon, K., Hutchinson, J.W., 2008. Modification of the gurson model for shear failure. European Journal of Mechanics-A/Solids 27, 1–17.

Nemat-Nasser, S., Isaacs, J.B., Liu, M., 1998. Microstructure of high-strain, high-strain-rate deformed tantalum. Acta Materialia 46, 1307–25.

Nesterenko, V.F., Bondar, M.P., 1994. Localization of deformation in collapse of a thick walled cylinder. Combustion, Explosion and Shock Waves 30, 500–9.

Nesterenko, V.F., Lazaridi, A.N., Pershin, S.A., 1989. Deformation localization in copper during explosive compression of hollow cylinders. The Physics of Combustion and Explosion 25, 154–5.

Nesterenko, V.F., Meyers, M.A., LaSalvia, J.C., Bondar, M.P., Chen, Y.J., Lukyanov, Y.L., 1997. Shear localization and recrystallization in high-strain, high-strain-rate deformation of tantalum. Materials Science and Engineering: A 229, 23–41.

Nesterenko, V.F., Meyers, M.A., Wright, T.W., 1995. Collective behavior of shear bands, in: Murr, L.E., Staudhammer, K.P., Meyers, M.A. (Eds.), Metallurgical and Materials Applications of Shock- Wave and High-Strain-Rate Phenomena, Elsevier Science B.V. pp. 397404.

Nesterenko, V.F., Meyers, M.A., Wright, T.W., 1998. Self-organization in the initiation of adiabatic shear bands. Acta materialia 46, 327–40.

Odeshi, A.G., Al-Ameeri, S., Mirfakhraei, S., Yazdani, F., Bassim, M.N., 2006. Deformation and failure mechanism in AISI 4340 steel under ballistic impact. Theoretical and Applied Fracture Mechanics 45, 18–24.

Osovski, S., Rittel, D., Landau, P., Venkert, A., 2012. Microstructural effects on adiabatic shear band formation. Scripta Materialia 66, 9–12.

Pascon, J.P., Waisman, H., 2021. A thermodynamic framework to predict ductile damage in thermoviscoplastic porous metals. Mechanics of Materials 153, 103701.

Peirs, J., Verleysen, P., Degrieck, J., Coghe, F., 2010. The use of hat-shaped specimens to study the high strain rate shear behaviour of Ti–6Al–4V. International Journal of Impact Engineering 37, 703–14. Impact Loading of Lightweight Structures.

Rittel, D., Landau, P., Venkert, A., 2008a. Dynamic recrystallization as a potential cause for adiabatic shear failure. Physical Review Letters 101, 165501.

Rittel, D., Lee, S., Ravichandran, G., 2002. A shear-compression specimen for large strain testing. Experimental Mechanics 42, 58–64.

Rittel, D., Wang, Z.G., Dorogoy, A., 2008b. Geometrical imperfection and adiabatic shear banding. International Journal of Impact Engineering 35, 1280–92.

Rusinek, A., Klepaczko, J.R., 2001. Shear testing of a sheet steel at wide range of strain rates and a constitutive relation with strain-rate and temperature dependence of the flow stress. International Journal of Plasticity 17, 87–115.

Rusinek, A., Zaera, R., 2007. Finite element simulation of steel ring fragmentation under radial expansion. International Journal of Impact Engineering 34, 799–822.

Schmitz, F., Winter, S., Clausmeyer, T., Wagner, M.F.X., Tekkaya, A.E., 2020. Adiabatic blanking of advanced high-strength steels. CIRP Annals 69, 269–72.

Schneider, C.A., Rasband, W.S., Eliceiri, K.W., 2012. Nih image to imagej: 25 years of image analysis. Nature methods 9, 671–5.

Shi, F.F., Merle, R., Hou, B., Liu, J.G., Li, Y.L., Zhao, H., 2014. A critical analysis of plane shear tests under quasi-static and impact loading. International Journal of Impact Engineering 74, 107–19. Advances in Impact Engineering: Selected papers from AEPA2012.

Stef, J., Poulon-Quintin, A., Redjaimia, A., Ghanbaja, J., Ferry, O., De Sousa, M., Gouné, M., 2018. Mechanism of porosity formation and influence on mechanical properties in selective laser melting of Ti-6Al-4V parts. Materials & Design 156, 480–93.

Stokes, J.L., Nesterenko, V.F., Shlachter, J.S., Fulton, R.D., Indrakanti, S.S., Gu, Y., 2001. Comparative behavior of Ti and 304 stainless steel in a magnetically-driven implosion at the pegasus-II facility. Fundamental issues and applications of shock-wave and high-strain-rate phenomena, (Proceedings of the EXPLOMET'2000). New York: Elsevier Science Ltd , 585–92.

Vural, M., Molinari, A., Bhattacharyya, N., 2011. Analysis of slot orientation in shear-compression specimen (SCS). Experimental mechanics 51, 263–73.

Vural, M., Ravichandran, G., Rittel, D., 2003. Large strain mechanical behavior of 1018 cold-rolled steel over a wide range of strain rates. Metallurgical and Materials Transactions A 34, 2873–85.

Wang, L.L., Bao, H.S., Lu, W.X., 1988. The dependence of adiabatic shear banding in strain-rate, strain and temperature. Journal de Physique Colloques 49, C3–207.

Wang, T., Liu, Z.L., Cui, Y.N., Ye, X., Liu, X.M., Tian, R., Zhuang, Z., 2020. A thermo-elastic-plastic phase-field model for simulating the evolution and transition of adiabatic shear band. Part II. Dynamic collapse of thick-walled cylinder. Engineering Fracture Mechanics 231, 107027.

Weck, A., Wilkinson, D.S., Toda, H., Maire, E., 2006. 2D and 3D visualization of ductile fracture. Advanced Engineering Materials 8, 469–72.

Wiehahn, M.A., Nurick, G.N., Bowles, H.C., 2000. Some insights into the mechanism of the deformation and tearing of thin plates at high strain rates incorporating temperature dependent material properties. WIT Transactions on the Built Environment 48.

Xu, Z., Ding, X., Zhang, W., Huang, F., 2017. A novel method in dynamic shear testing of bulk materials using the traditional shpb technique. International Journal of Impact Engineering 101, 90–104.

Xu, Z., Liu, Y., Hu, H., He, X., Huang, F., 2019a. Determination of shear behavior and constitutive modeling of the 603 steel over wide temperature and strain rate ranges. Journal of the Mechanics and Physics of Solids 129, 184–204.

Xu, Z., Liu, Y., Hu, H., He, X., Huang, F., 2019b. Thermo-viscoplastic behavior and constitutive modeling of pure copper under high-strain-rate shear condition. Mechanics of Materials 129, 306–19.

Xu, Z., Liu, Y., Sun, Z., Hu, H., Huang, F., 2018. On shear failure behaviors of an armor steel over a large range of strain rates. International Journal of Impact Engineering 118, 24–38.

Xue, Q., Meyers, M.A., Nesterenko, V.F., 2002. Self-organization of shear bands in titanium and Ti–6Al–4V alloy. Acta materialia 50, 575–96.

Xue, Q., Meyers, M.A., Nesterenko, V.F., 2004. Self organization of shear bands in stainless steel. Materials Science and Engineering: A 384, 35–46.

Yang, Y., Jiang, L., 2016. Self-organization of adiabatic shear bands in ZK60 magnesium alloy. Materials Science and Engineering: A 655, 321–30.

Yang, Y., Jiang, L., Xu, Z., Wang, Z., 2017. An examination of adiabatic shearing behavior in ZK60 alloy with different states of heat treatment. Materials Science and Engineering: A 685, 57–64.

Yang, Y., Zheng, H.G., Zhao, Z.D., Zhang, Q., Zhang, Q.M., Jiang, F., Li, X.M., 2011. Effect of phase composition on self-organization of shear bands in Ti-1300 titanium alloy. Materials Science and Engineering: A 528, 7506–13.

Ye, G.G., Xue, S.F., Jiang, M.Q., Tong, X.H., Dai, L.H., 2013. Modeling periodic adiabatic shear band evolution during high speed machining Ti-6Al-4V alloy. International Journal of Plasticity 40, 39–55.

Zaera, R., Rodríguez-Martínez, J.A., Vadillo, G., Fernández-Sáez, J., Molinari, A., 2015. Collective behaviour and spacing of necks in ductile plates subjected to dynamic biaxial loading. Journal of the Mechanics and Physics of Solids 85, 245–69.

Zener, C., Hollomon, J.H., 1944. Effect of strain rate upon plastic flow of steel. Journal of Applied Physics 15, 22–32.

Zhang, L., Pellegrino, A., Townsend, D., Petrinic, N., 2021. Thermomechanical constitutive behaviour of a near α titanium alloy over a wide range of strain rates: Experiments and modelling. International Journal of Mechanical Sciences 189, 105970.

Zhou, M., Ravichandran, G., Rosakis, A.J., 1996b. Dynamically propagating shear bands in impact-loaded prenotched plates—II. Numerical simulations. Journal of the Mechanics and Physics of Solids 44, 1007–32.

Zhou, M., Rosakis, A.J., Ravichandran, G., 1996a. Dynamically propagating shear bands in impact-loaded prenotched plates—I. Experimental investigations of temperature signatures and propagation speed. Journal of the Mechanics and Physics of Solids 44, 981–1006.

Zou, D.L., Zhen, L., Xu, C.Y., Shao, W.Z., 2011. Characterization of adiabatic shear bands in AM60B magnesium alloy under ballistic impact. Materials characterization 62, 496–502.